



OPEN

# Efficient MoWO<sub>3</sub>/VO<sub>2</sub>/MoS<sub>2</sub>/Si UV Schottky photodetectors; MoS<sub>2</sub> optimization and monoclinic VO<sub>2</sub> surface modifications

Mohamed A. Basyooni<sup>1,5</sup>, Shrouk E. Zaki<sup>1</sup>, Mohamed Shaban<sup>2,3</sup>✉, Yasin Ramazan Eker<sup>4,5</sup> & Mucahit Yilmaz<sup>1</sup>

The distinctive properties of strongly correlated oxides provide a variety of possibilities for modulating the properties of 2D transition metal dichalcogenides semiconductors; which represent a new class of superior optical and optoelectronic interfacing semiconductors. We report a novel approach to scaling-up molybdenum disulfide (MoS<sub>2</sub>) by combining the techniques of chemical and physical vapor deposition (CVD and PVD) and interfacing with a thin layer of monoclinic VO<sub>2</sub>. MoWO<sub>3</sub>/VO<sub>2</sub>/MoS<sub>2</sub> photodetectors were manufactured at different sputtering times by depositing molybdenum oxide layers using a PVD technique on p-type silicon substrates followed by a sulphurization process in the CVD chamber. The high quality and the excellent structural and absorption properties of MoWO<sub>3</sub>/VO<sub>2</sub>/MoS<sub>2</sub>/Si with MoS<sub>2</sub> deposited for 60 s enables its use as an efficient UV photodetector. The electronically coupled monoclinic VO<sub>2</sub> layer on MoS<sub>2</sub>/Si causes a redshift and intensive MoS<sub>2</sub> Raman peaks. Interestingly, the incorporation of VO<sub>2</sub> dramatically changes the ratio between A-exciton (ground state exciton) and trion photoluminescence intensities of VO<sub>2</sub>/(30 s)MoS<sub>2</sub>/Si from < 1 to > 1. By increasing the deposition time of MoS<sub>2</sub> from 60 to 180 s, the relative intensity of the B-exciton/A-exciton increases, whereas the lowest ratio at deposition time of 60 s refers to the high quality and low defect densities of the VO<sub>2</sub>/(60 s)MoS<sub>2</sub>/Si structure. Both the VO<sub>2</sub>/(60 s)MoS<sub>2</sub>/Si trion and A-exciton peaks have higher intensities compared with (60 s) MoS<sub>2</sub>/Si structure. The MoWO<sub>3</sub>/VO<sub>2</sub>/(60 s) MoS<sub>2</sub>/Si photodetector displays the highest photocurrent gain of 1.6,  $4.32 \times 10^8$  Jones detectivity, and  $\sim 1.0 \times 10^{10}$  quantum efficiency at 365 nm. Moreover, the surface roughness and grains mapping are studied and a low semiconducting-metallic phase transition is observed at  $\sim 40$  °C.

The current experiments of integrating 2D TMDCs into nano-electronic devices such as MoS<sub>2</sub>, WS<sub>2</sub>, and black phosphorous still have challenges like low carrier mobility and low photoluminescence (PL) efficiency which limit their further applications in optoelectronics. It is believed that in 2D TMDCs, the Van der Waals (VDWs) interlayer forces are weak and little defects can enhance the intrinsic phonon scattering and lead to better electrical conduction. Charge traps in 2D TMDCs are found to have a direct relationship with the carrier mobility and the output resistances of the electronic devices<sup>1</sup>. Therefore, in order to enhance the Raman intensity, PL intensity, and the charge carrier mobility of the optoelectronic devices, either by an interfacing functional channel material or a functional substrate that modulates the device output in multiple ways, many functional oxides have been used to offer unique properties such as piezoelectricity, strong polarization, and spin injection.

Chemical vapor deposition (CVD) is widely thought to be the most common method for preparing MoS<sub>2</sub>. In which MoO<sub>3</sub> and sulfur powders are utilized with some inert gases through two or three-zone quartz tubes.

<sup>1</sup>Nanophysics Laboratory, Department of NanoScience and NanoEngineering, Institute of Science and Technology, University of Necmettin Erbakan, Konya 42060, Turkey. <sup>2</sup>Nanophotonics and Applications Laboratory, Department of Physics, Faculty of Science, Beni-Suef University, Beni Suef 62514, Egypt. <sup>3</sup>Department of Physics, Faculty of Science, Islamic University in Almadinah Almonawara, Almadinah Almonawara 42351, Saudi Arabia. <sup>4</sup>Department of Metallurgy and Material Engineering, Faculty of Engineering and Architecture, Necmettin Erbakan University, Konya 42060, Turkey. <sup>5</sup>Science and Technology Research and Application Center (BITAM), University of Necmettin Erbakan, Konya 42060, Turkey. ✉email: mssfadel@aucegypt.edu

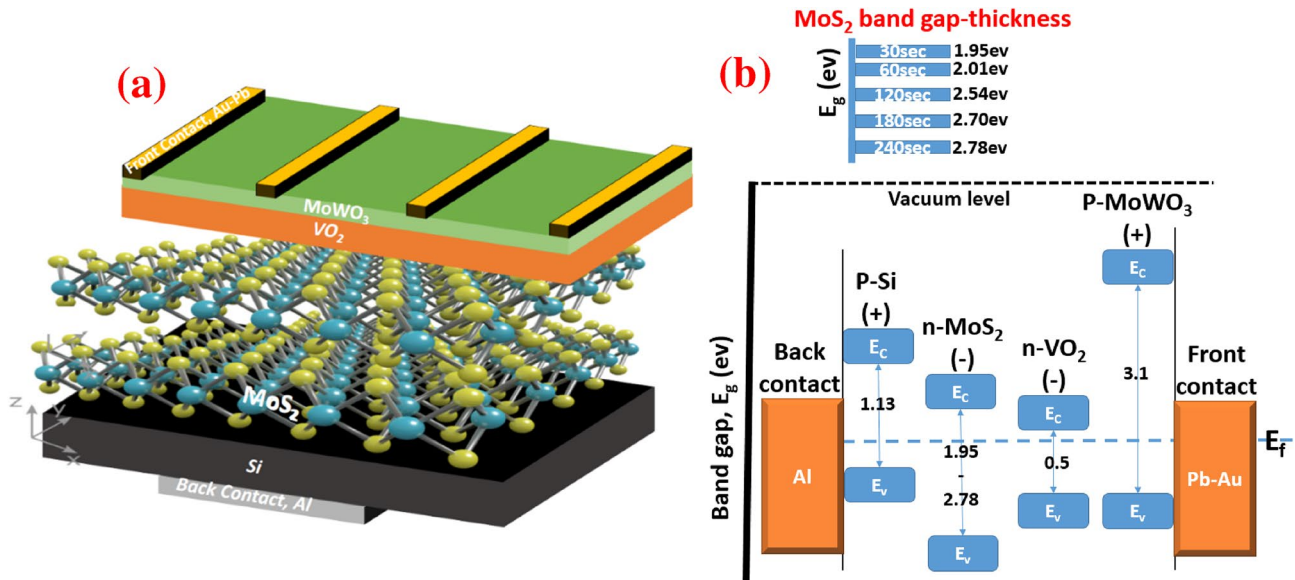


**Figure 1.** (a) schematic diagram of the proposed  $\text{MoWO}_3/\text{VO}_2/\text{MoS}_2/\text{Si}$  UV photodetector and (b) its band alignment with different Mo-O sputtering time (30–240 s).

The substrate can be maintained at downstream gas flow to grow  $\text{MoS}_2$ <sup>2–4</sup>. Nevertheless, this growth technique has several disadvantages through which non-homogenous, tiny flakes, and 2D  $\text{MoS}_2$  in the micro/nanoscale is formed. These disadvantages restrict its application in the industrial optoelectronic devices. On the other hand, methods such as exfoliation approaches, "top-down," have been used to prepare 2D sheets of graphene,  $\text{MoS}_2$ , etc. This method including different forms such as micromechanical exfoliation<sup>5</sup>, sonication-assisted liquid-exfoliation<sup>6–8</sup>, shear exfoliation<sup>9,10</sup> and chemical exfoliation<sup>11,12</sup>. Micromechanical exfoliation still has some disadvantages such as low quality, small-scale production, and high amount of defects<sup>13</sup>. Another drawback is that the exfoliated  $\text{MoS}_2$  must be transferred to a new substratum that handles its scaling and mass production<sup>14</sup>. Nonetheless, for the next generation of optoelectronics and quantum computers, the demand for wafer-scale and homogeneous 2D materials such as  $\text{MoS}_2$  has increased in recent years. Mainly, these methods including atomic layer deposition (ALD)<sup>14,15</sup>, pulsed laser deposition (PLD)<sup>16,17</sup>, thermal evaporation<sup>18,19</sup>, and magnetron sputtering techniques<sup>20–22</sup>. Magnetron sputtering was commonly employed at low cost and with easy control in large-scale for commercial manufacturing.

Strongly correlated oxides are a wide range of materials where the associated electronic, magnetic properties, and spin are strongly correlated with each other. The local spin density approximation (LSDA) has been used to determine the energy band structure of many kinds of materials. However, the LSDA fails to describe the electronic structure of some materials in which the interaction among the electrons is strong (e–e interaction) such as strongly correlated electron systems<sup>23</sup>. Meanwhile, the dominant role of the Coulomb repulsion forces between the electrons in  $\text{VO}_2$  and  $\text{V}_2\text{O}_3$  systems is opening the insulating gap<sup>24,25</sup>. However, when strongly correlated oxides interface with 2D TMDCs, multi-functions such as bandgap, charge transfer, energy transfer, and strain can be tuned<sup>26,27</sup>. Among them, vanadium dioxide ( $\text{VO}_2$ ); an archetypal strongly correlated functional oxide that exhibits a metal–insulator transition (MIT) above room temperature. At ambient pressure, below the transition temperature ( $T_c$ ),  $\text{VO}_2$  has a monoclinic (M1 phase), with space group  $P2_1/c(\#14)$ <sup>28</sup> and lattice constant of  $a \approx 5.75\text{\AA}$ ,  $b \approx 4.53\text{\AA}$ ,  $c \approx 5.38\text{\AA}$ ,  $\beta = 122.6^\circ$ <sup>29,30</sup>. Above the  $T_c$ ,  $\text{VO}_2$  adopts a tetragonal rutile (R) structure with space group  $P4_2mm(\#136)$  and a lattice constants  $a = b \approx 4.55\text{\AA}$ ,  $c \approx 2.85\text{\AA}$ <sup>30</sup>.

Due to the superior physical properties at the interface between  $\text{MoS}_2$  and  $\text{VO}_2$  layer, the manufacture of  $\text{MoS}_2/\text{VO}_2$  heterostructure for optoelectronic devices has received considerable attention. However, for optical and optoelectronic products, account should be taken of the manufacturing process of homogenous and scaled-up  $\text{MoS}_2$ . Oliva et al. reported the design of Van der Waals  $\text{MoS}_2/\text{VO}_2$  photodetector<sup>31</sup>. Nevertheless, in that report, the manufacturing process of  $\text{MoS}_2$  includes several steps related to the micromechanical exfoliation process. The photo-excited carriers transfer in  $\text{MoS}_2$  and  $\text{VO}_2$  was studied, whereas the CVD powder vaporization technique was used for the growth of small flakes of  $\text{MoS}_2$ <sup>32</sup>. However, for the easy production of scalable and homogenous  $\text{MoS}_2$ -based industrial applications, controllability and optimization of deposition time and growth parameters are highly required. Here, we report the preparation, characterization, and optoelectronic application of  $\text{MoWO}_3/\text{VO}_2/\text{MoS}_2/\text{Si}$  (p–n–n–p) structure towards 365 nm photodetector at room temperature. Different sputtering times of Mo–O have been controlled followed by sulfurization process and interfacing with a monoclinic  $\text{VO}_2$  layer. Figure 1a shows a schematic diagram of the proposed  $\text{MoWO}_3/\text{VO}_2/\text{MoS}_2/\text{Si}$  (p–n–n–p) photodetector. Note that most of the previously reported studies were trying to enhance the Raman, PL, optoelectronic of  $\text{VO}_2$ – $\text{MoS}_2$  by controlling the device temperature. However, these attempts did not relay for low temperature-phase transition optoelectronic devices. Here, this study focuses on the surface coupling and strain-induced optoelectronic modulation on a few-layer  $\text{VO}_2/\text{MoS}_2/\text{Si}$  heterostructure. Figure 1b shows the band alignment of the optimized p–n–n–p-type structure with different Mo–O sputtering times to control the  $\text{MoS}_2$

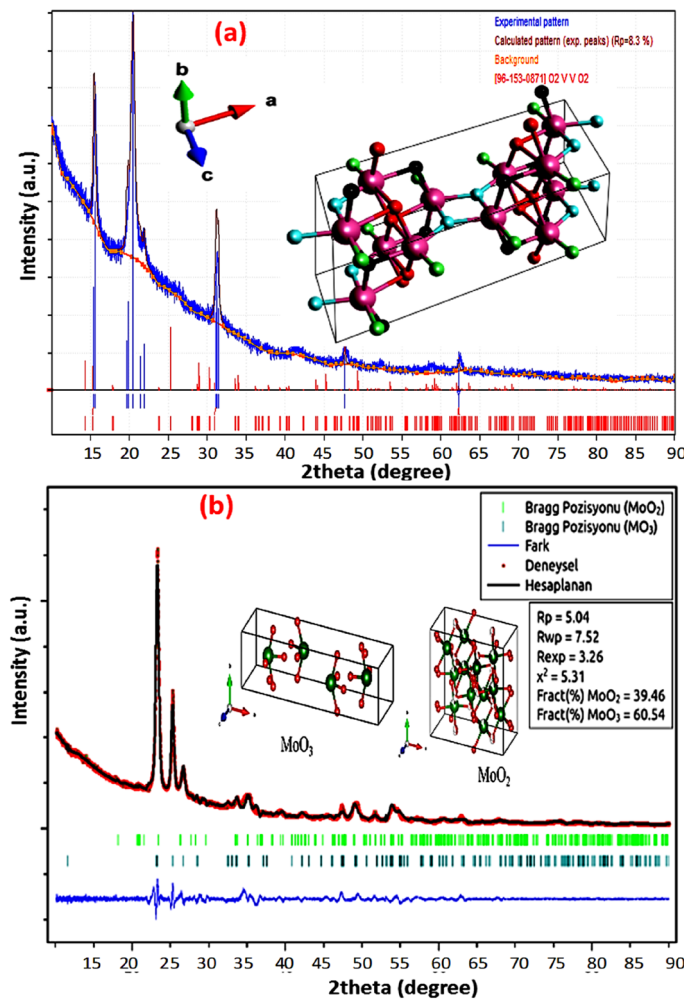


**Figure 2.** XRD crystal structure of (a) monoclinic VO<sub>2</sub> and (b) Rietveld structure refinement XRD pattern of molybdenum oxide (in our case MoO<sub>2</sub> and MoO<sub>3</sub>). The inserted 3D crystal structures are obtained using VESTA 3D visualization program (Model VESTA 3; <https://jp-minerals.org/vesta/en/>).

bandgap<sup>33</sup>. The nanostructured thin layer of Mo<sub>0.2</sub>W<sub>0.8</sub>O<sub>3</sub> was deposited on the surface of VO<sub>2</sub> as a protective and anti-reflection layer<sup>34</sup>. The optical anti-reflective layer (Mo<sub>0.2</sub>W<sub>0.8</sub>O<sub>3</sub>) is used to improve the responsivity of the photodetector and strongly eliminate the optical interference to minimize its undesired effects. Numerous applications including photodiodes<sup>35</sup>, image sensor<sup>36</sup>, and semiconductor photodetectors<sup>37</sup> have recorded the uses of the antireflective coating. The structural and morphological characteristics are also studied here. Raman, PL, electrical, optoelectronic characterization of strongly correlated oxide (VO<sub>2</sub>), and 2D VDW heterostructure (MoS<sub>2</sub>-Si) will be discussed.

## Results and discussion

**Structural and composition.** The crystal structure of vanadium oxide and molybdenum oxide was calculated in detail to understand the structural analysis of the deposited films. Figure 2a shows the XRD pattern of the deposited VO<sub>2</sub> thin film. XRD result of VO<sub>2</sub> shows a monoclinic phase with a JCPDS card number of [#96-153-0871] with a space group of C12/m<sub>1</sub>(12). The inserted crystal structure and visualizing 3D data are obtained using VESTA crystal software. Different diffraction peaks are observed at  $2\theta = 15.45^\circ, 20.49^\circ, 31.28^\circ, 47.69^\circ$ , and  $62.32^\circ$ . The unit cell parameters are  $a = 12.03000 \text{ \AA}$ ,  $b = 3.69300 \text{ \AA}$ ,  $c = 6.42000 \text{ \AA}$  while the angle is  $\beta = 106.100^\circ$ . However, the Wyckoff position of metal atoms are (2a): (0, 0, 0) and (4f): (0.25, 0.25, 0.25) and oxygen atoms are (4i): (0.175, 0, 0.25), (0.175, 0.5, 0.25) and (8j): (0.075, 0.25, 0.75). The calculated amount of O:V in the VO<sub>2</sub> compound indicating that more oxygen vacancies. Oxygen deficient in vanadium oxide (VO<sub>2-δ</sub>) has reported many times to stabilize the metallic state of VO<sub>2</sub><sup>38</sup>, decrease the semiconductor–metal phase transition (SMT)<sup>39</sup> as reported here and to narrow the bandgap in the monoclinic phase<sup>40</sup>. Oxygen vacancies are acting as an electron donor with n-type conductivity which can change the electron orbital occupancy, band structures, and contribute to high photocurrent gain when stacking with MoS<sub>2</sub><sup>41</sup>.

The preparation of molybdenum oxide was achieved using the Mo target at sputtering temperature of 400 °C. Figure 2b shows the XRD Rietveld refinement of Mo-O bonding in molybdenum oxide. The calculated R-factors were found to be  $R_{wp} = 7.52$ ,  $R_{exp} = 3.26$ , and  $\chi^2 = 25.31$ . The Refinement analysis shows that MoO<sub>3</sub> and MoO<sub>2</sub>

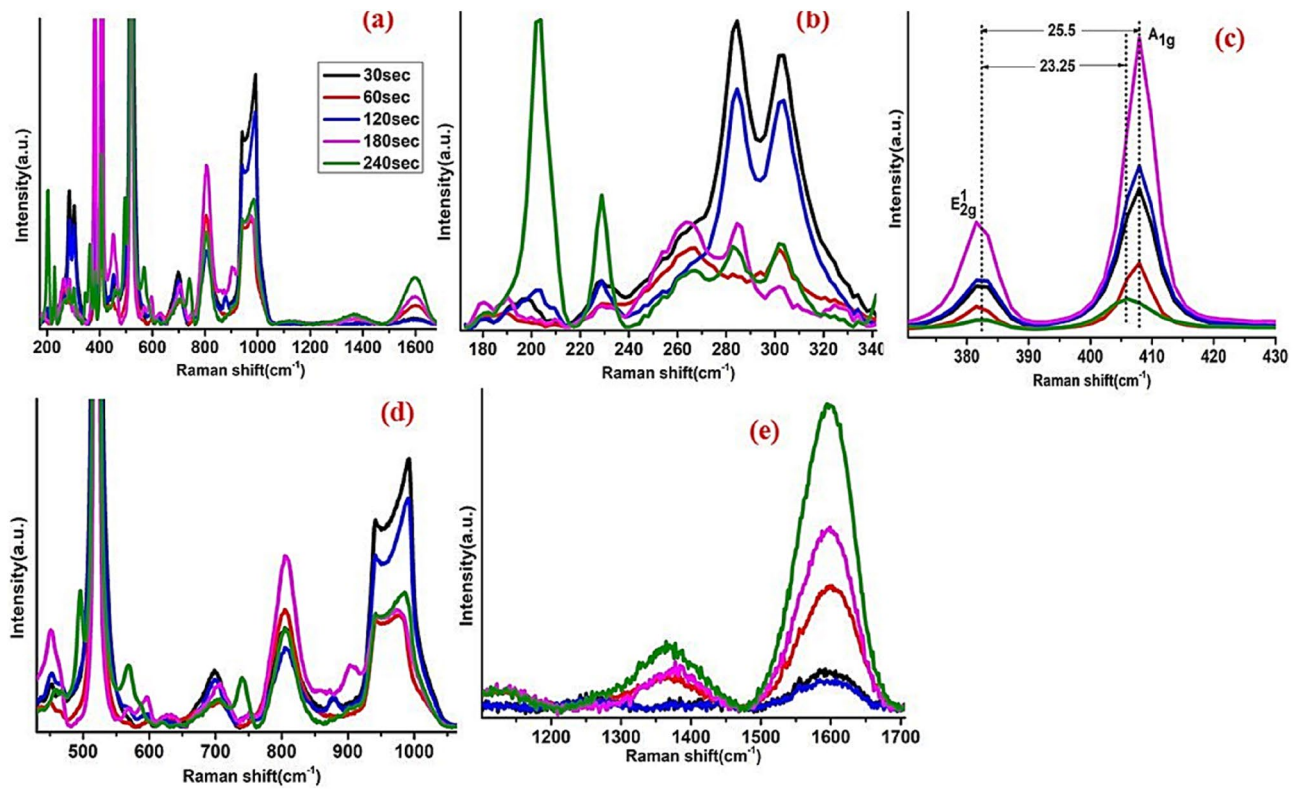


**Figure 3.** Raman spectra of the deposited multilayer  $\text{MoWO}_3/\text{VO}_2/\text{MoS}_2$  on p-type Si substrate; (a) the full range ( $200\text{--}1700\text{ cm}^{-1}$ ) Raman spectra of the deposited films; (b–e) magnified ranges of the full range spectra.

Deposition time	30 s		60 s		120 s		180 s		240 s	
VO <sub>2</sub> layer	With	Without	With	Without	With	Without	With	Without	With	Without
Position of $E_{2g}^1$ ( $\text{cm}^{-1}$ )	382.02	384.91	382.16	385.26	382.49	385.93	381.51	385.51	382.51	385.39
Position of $A_{1g}$ ( $\text{cm}^{-1}$ )	407.73	410.03	407.61	410.22	407.80	410.39	409.86	410.80	406.14	409.79
Position difference ( $E_{2g}^1 - A_{1g}$ ) ( $\text{cm}^{-1}$ )	25.71	25.12	25.44	24.96	25.31	24.46	28.31	25.28	23.63	24.40
Intensity of $E_{2g}^1$	110,852.8	22,177.5	204,858.9	39,921.1	231,297.2	71,156.9	503,416.9	191,107.0	45,413.2	120,485.6
Intensity of $A_{1g}$	313,824.8	60,847.9	664,071.8	113,963.2	762,847.3	180,168.1	1,364,933.3	465,300.5	144,965.8	240,574.3
Intensity difference ( $E_{2g}^1 - A_{1g}$ )	202,972.0	38,670.4	459,212.9	74,042.1	531,550.1	109,011.2	861,516.4	274,193.5	99,552.6	120,088.7

**Table 1.** The Raman peaks positions and intensities of  $\text{VO}_2/\text{MoS}_2/\text{Si}$  and  $\text{MoS}_2/\text{Si}$  structures.

crystal phases are contributed. The distribution of atoms in unit cells of  $\text{MoO}_2$  and  $\text{MoO}_3$  was plotted with the VESTA program and shown in Fig. 2b. The amounts of Mo in  $\text{MoO}_2$  and  $\text{MoO}_3$  were calculated as 1.837 and 1, respectively. While the amounts of O<sub>2</sub> in  $\text{MoO}_2$  and  $\text{MoO}_3$  were 3.836 and 3.012, respectively. The calculation of the crystal structure was showed that 9.46% as  $\text{MoO}_2$  phase and 54% as  $\text{MoO}_3$  phase. Moreover, the unit cell parameters of the  $\text{MoO}_2$  structure are  $a = 9.788$ ,  $b = 8.604$ ,  $c = 4.714\text{ \AA}$ . While for  $\text{MoO}_3$  structure are  $a = 15.309$ ,  $b = 3.719$ ,  $c = 3.976\text{ \AA}$ .

**Raman characterization.** The physics behind interfacing structures such as 2D semiconductors and correlated oxides should receive high attention. The importance of these structures can be highlighted by controlling the band alignment of the 2D materials such as  $\text{MoS}_2$ . Moreover, controlling the carrier mobility, coupling, and strain effect (as reported in the current work)<sup>42</sup>. Raman spectra of the deposited multilayer structure  $\text{MoWO}_3/\text{VO}_2/\text{MoS}_2$  on p-type Si substrate are depicted in Fig. 3. The full range ( $200\text{--}1700\text{ cm}^{-1}$ ) Raman spectra of the deposited structures are shown in Fig. 3a and the magnified ranges of the full range spectra are shown in Fig. 3b–e. The Raman peaks of  $\text{VO}_2$  at RT are shown in Fig. 3a,b,d which confirm its monoclinic phase. Whereas, Fig. 3c shows the two characteristic peaks of  $\text{MoS}_2$  of  $E_{2g}^1$  ( $385\text{ cm}^{-1}$ ) and  $A_{1g}$  ( $405\text{ cm}^{-1}$ ) originate from their in-plane and out-of-plane phonon characteristics<sup>43</sup>. The peaks positions, intensities, distance between  $E_{2g}^1$  and  $A_{1g}$  position at different sputtering time of  $\text{MoS}_2$  are summarized in Table 1 and Fig. 4.

Many authors tried to study the effect of  $\text{VO}_2$  in contact with transition metal dichalcogenides semiconductors (TMDs) layers such as  $\text{MoS}_2$  and  $\text{WS}_2$ <sup>31,32</sup>. While in our current study, we tried to study the matching behavior

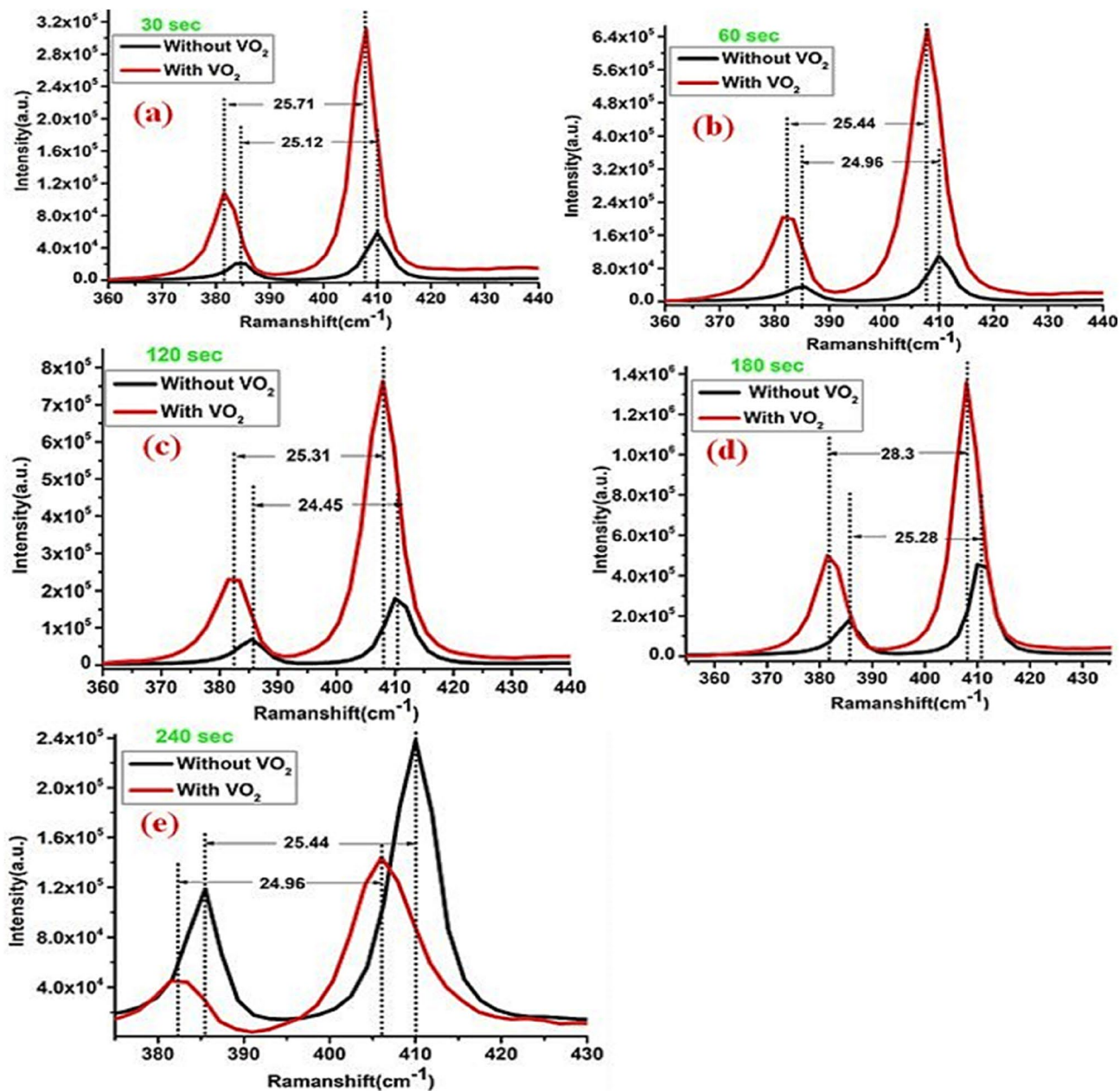


**Figure 4.** Raman peaks of MoS<sub>2</sub>/Si fabricated at different sputtering times in the presence and absence of VO<sub>2</sub> layer on the surface.

of 50 nm thin VO<sub>2</sub> layer onto the surface of MoS<sub>2</sub>/Si heterojunction. Additionally, the current work showed that different thicknesses of Mo-O structure have a direct effect on Raman, PL, electrical and optoelectronic characterization of MoS<sub>2</sub> peaks (position and intensity). It is seen from Raman spectra that with incorporated the monoclinic VO<sub>2</sub> layer, there is a redshift and an increase in the intensity peaks as in Fig. 4a–d. These observations showed that MoS<sub>2</sub> and VO<sub>2</sub> were electronically coupled, similar results observed before<sup>32</sup>. The observed shift in Raman modes may be attributed to the presence of compressive strain induced by implementing the VO<sub>2</sub> layer, similar results observed when interfacing MoS<sub>2</sub> with PMN-PT<sup>44</sup>. Generally, compression stress exerted on VDWs structure decreases the lattice constant<sup>44,45</sup> and consequently increases the film crystallinity and photocurrent as reported here.

It is known that the intensity of Raman peaks is referring to high crystallinity effects. In most cases, Raman scattering is sensitive to the degree of crystallinity in a sample. Typically a crystalline material yields a spectrum with very sharp, intense Raman peaks, whilst an amorphous material will show less intense Raman peaks<sup>46–48</sup>. Table 1 and Fig. 4 show the Raman intensities of the corresponding thin films. These results show high attention to the applications of enhancing the Raman signal/intensity. The difference between peak positions of E<sub>2g</sub><sup>1</sup> and A<sub>1g</sub> in the presence and absence of VO<sub>2</sub> layer are deposited in Table 1. It shows a decrease with increasing the MoS<sub>2</sub> layer thickness from 30 to 240 s for both MoS<sub>2</sub>/Si and VO<sub>2</sub>/MoS<sub>2</sub>/Si structures, which may contribute to

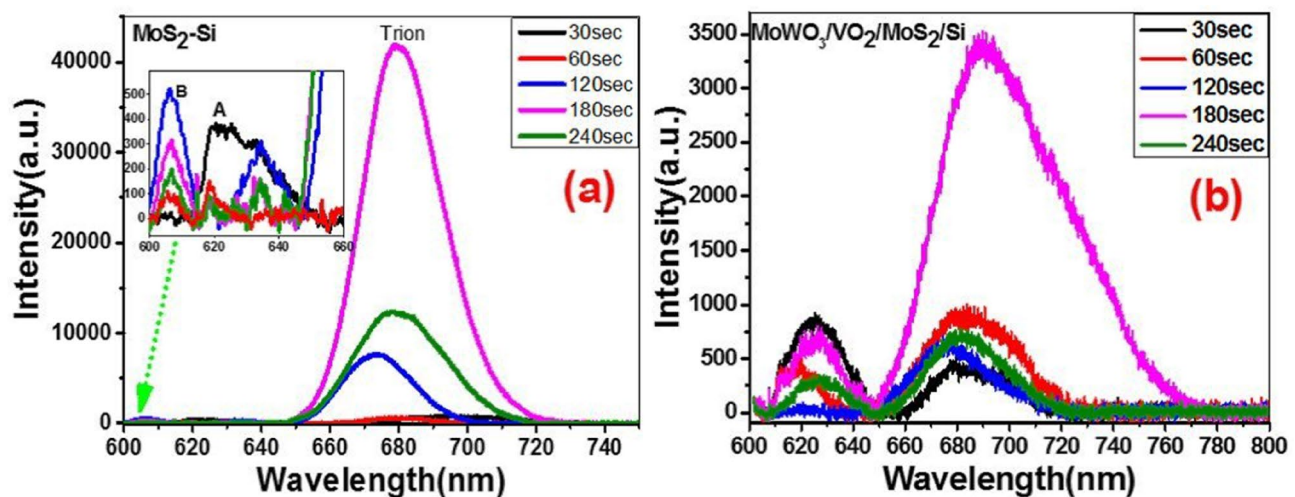


**Figure 5.** PL spectra of (a)  $\text{MoS}_2$ -Si heterojunction and (b)  $\text{MoWO}_3/\text{VO}_2/\text{MoS}_2$ -Si photodetectors.

a decrease in the film layers and enhance the band gap<sup>49</sup> as seen from Table 1. However, the film deposited at 180 s is out of this base. Meanwhile, the differences between the intensities of the peaks show an enhancement in the peak intensity with increasing the  $\text{MoS}_2$  film thickness which may contribute to high crystallinity effects. In counter, the film deposited at 240 s shows a decrease in the intensity. The highest intensity was observed for  $\text{VO}_2/\text{MoS}_2/\text{Si}$  with 180 s, whereas the lowest intensity was attributed to 240 s film. These results are concluded that the  $\text{MoS}_2$  sputtering time of 180 s is optimized for  $\text{VO}_2$  and  $\text{MoS}_2$  optical coupling. Consequently, the observed results may highlight the importance of incorporating strongly correlated oxide through 2D VDWs  $\text{MoS}_2$  structure to control film crystallinity, surface-enhanced Raman spectroscopy (SERS) of  $\text{MoS}_2$  for better signal detection and spatial resolution<sup>50–52</sup>, optical coupling<sup>53,54</sup>, Plasmonic local-field enhancement<sup>55</sup> and optoelectronic behavior<sup>51</sup>.

For more details about intensity distribution versus position, Raman mappings of  $E_{2g}^1$ ,  $A_{1g}$  and Si peaks of  $\text{MoS}_2/\text{Si}$  at different sputtering time of Mo-O (30, 60, 120, 180, and 240 s) are investigated at 385, 410, and  $520\text{ cm}^{-1}$ , respectively, and shown in Fig. S3 (a, b, c, d, and e). The Raman mapping was realized at large area ( $1.6\text{ mm} \times 1\text{ mm}$ ) with  $320 \times 200$  data point using Leica microscope at  $5\times$  magnification to provide an evidence about the ability to scale up the  $\text{MoS}_2$  thin films. The wavelength, power and integration time of the used laser were  $532\text{ nm}$ ,  $3\text{ mW}$  and  $1\text{ s}$ , respectively. This analysis illustrated that 30, 60, and 120 s samples show high homogeneity over the full scale ( $1.6 \times 1\text{ mm}^2$ ). Although, 180 s sample shows regular agglomerations of nanoparticles for both  $E_{2g}$  and  $A_{1g}$  positions, the 240 s sample shows irregular clusters. The scaling up of  $\text{MoS}_2$  can therefore be demonstrated until sputtering time  $< 180$  min.

**Photoluminescence measurements (PL).** The PL spectrum of  $\text{MoS}_2$  is strongly dependent on the number of layers of 2D VDWs structures. In other words, a strong PL peak may observe in single-layer  $\text{MoS}_2$  or  $\text{WS}_2$  film and decreasing with increasing the number of layers<sup>55</sup>. Trion is defined as a quasi-particle that can potentially carry out more information and data than electrons for which make them useful towards different applications such as optoelectronics and quantum computing<sup>56</sup>. Trions are consisting of three charged particles bound together by very weak bonding energy that makes them quickly fall apart<sup>57</sup>. It is known that the dominated peak in Figs. 5 and 6 attributed to the recombination of the photogenerated electron–hole pair, whereas the observed weaker peak at lower wavelength may be attributed to the valance band splitting due to the presence of strong spin-orbit coupling of  $\text{MoS}_2$ <sup>58</sup>. In the literature review, the definition of trion and exciton peak is dominated by their locations and the trion peak is located at lower energy than exciton peak<sup>59–61</sup>. Figure 5a and b shows the PL spectra of  $\text{MoS}_2/\text{Si}$  and  $\text{MoWO}_3/\text{VO}_2/\text{MoS}_2/\text{Si}$  structures at RT. The  $\text{MoS}_2/\text{Si}$  has two peaks at  $\sim 679$  and  $\sim 620\text{ nm}$  which corresponding to components from trion and A-exciton<sup>62</sup>. However, trion and A-exciton positions have changed by controlling the deposition time of  $\text{MoS}_2$  as seen in Table 2. Also, this table shows the position of the characteristic peaks (A-exciton, B-exciton (higher spin-orbit splitting state), and trion) in the presence and absence of the  $\text{VO}_2$  layer. Generally, it is seen that the trion peak shifted to lower energy by implementing the  $\text{VO}_2$  layer onto the surface of the  $\text{MoS}_2/\text{Si}$  structure as seen in Table 2.

The A-exciton peak has a higher intensity in the case of the  $\text{VO}_2/\text{MoS}_2/\text{Si}$  structure than in the case of  $\text{MoS}_2/\text{Si}$  structure for 30 and 60 s deposition time of  $\text{MoS}_2$  layer, Fig. 6a and b. The trion peak is enhanced and shifted to longer wavelengths by increasing the deposition time to 60 s. The increase in PL intensity refers to an enhancement in light emission efficiency and increases the density of states of the photo carriers by modifying the band structure<sup>44</sup>. At 30 s, the A-exciton peak intensity is higher for the  $\text{VO}_2/\text{MoS}_2/\text{Si}$  structure than the  $\text{MoS}_2/\text{Si}$  structure. i.e., the incorporation of  $\text{VO}_2$  dramatically changes the ratio between photoluminescence intensities of A-exciton and trion from  $< 1$  to  $> 1$  for  $\text{VO}_2/(30\text{ s})\text{MoS}_2/\text{Si}$  structure. However, the opposite case is observed for the trion. Meanwhile, by incorporating the  $\text{VO}_2$  layer, a blue shift in the trion peak is observed, while a redshift is observed for the A-excitons. The observed peak position of PL that shifted towards lower energy (redshift) attributed to the non-radiative electron–hole recombination effect. However, by increasing the deposition time to 60 s, the A-exciton peak have higher intensity compared with the trions peak in the case of  $\text{VO}_2/\text{MoS}_2/\text{Si}$

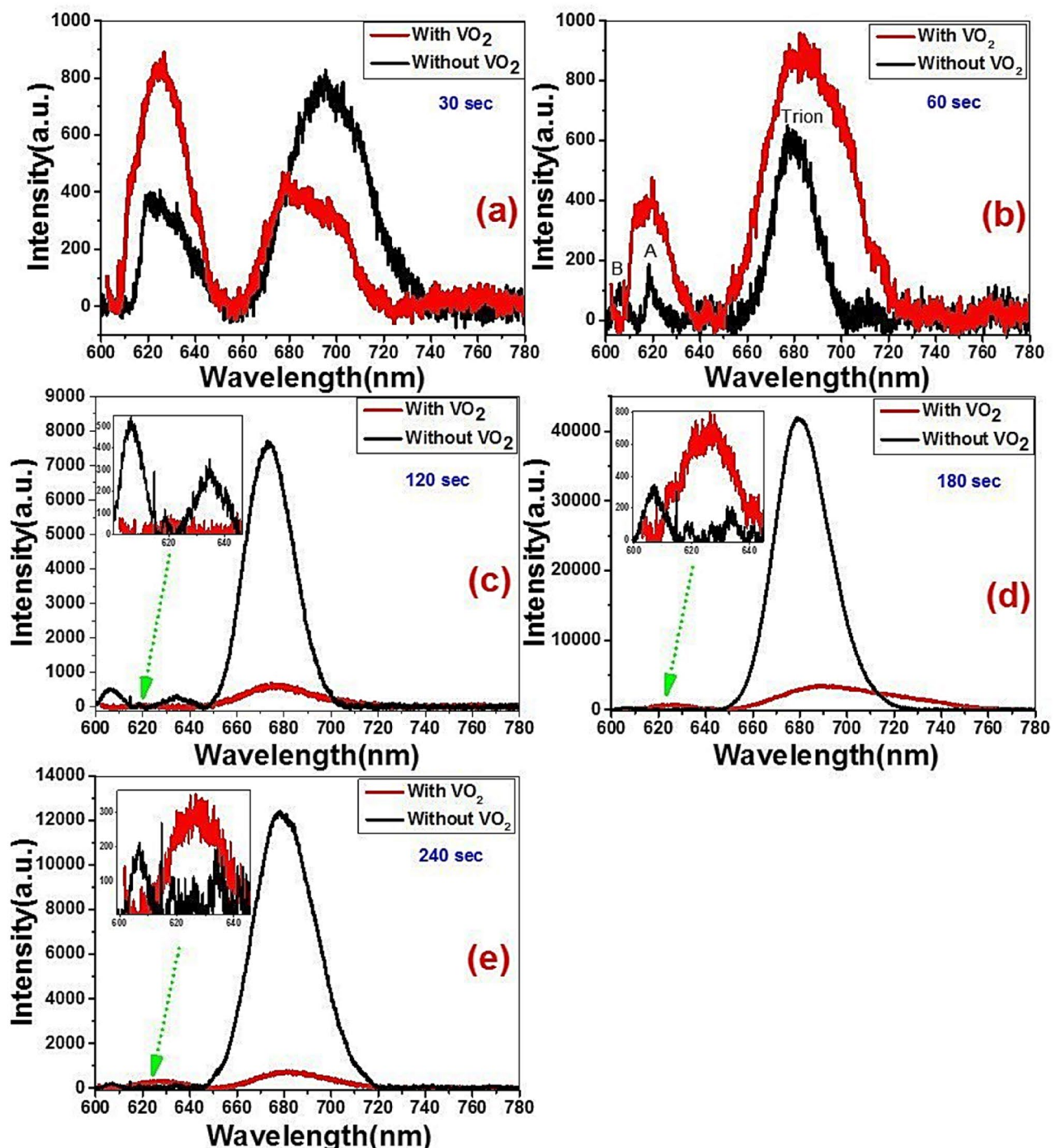


**Figure 6.** PL spectra of MoS<sub>2</sub>/Si fabricated at different sputtering times without and with VO<sub>2</sub> supporting layer on the surface.

structure than MoS<sub>2</sub>/Si structure as seen in Fig. 6b. By increasing the deposition time of MoS<sub>2</sub> from 60 to 180 s, the B-exciton/A-exciton relative intensity increases, whereas the lowest ratio at 60 s deposition time refers to the high quality and the low defects densities of VO<sub>2</sub>/(60 s) MoS<sub>2</sub>/Si structure. Moreover, a redshift was observed for the trion peak and a slight blue shift when incorporating the VO<sub>2</sub> layer. The increase in PL intensity refers to an enhancement in light emission efficiency and increases the density of states of the carriers by modifying the band structure and consequently enhance the radiative recombination of carriers, similar results were observed in a compressively strained trilayer MoS<sub>2</sub> sheet<sup>44,63,64</sup>. This result shows that strong coupling between VO<sub>2</sub> and MoS<sub>2</sub> at 60 s Mo-O deposition time was observed at room temperature. While the PL intensity with MoS<sub>2</sub>/VO<sub>2</sub> structure has only enhanced with increasing the film temperature<sup>31,32,65</sup>, while our reported results show a dramatic enhancement in the PL intensity at RT by incorporating VO<sub>2</sub> layer on the surface of MoS<sub>2</sub>/Si structure.

MoO <sub>3</sub> deposition time	30 s		60 s		120 s		180 s		240 s	
VO <sub>2</sub> layer	With	Without	With	Without	With	Without	With	Without	With	Without
<b>Peak position (nm)</b>										
Trion	678.65	696.06 Blue shift	682.47	679.32 Red shift	676.29	673.08 Red shift	690.40	679.54 Red shift	681.32	678.78 Red shift
A-exciton	625.08	622.21 Red shift	617.20	618.11 Blue shift	602.82	634.7 Blue shift	624.97	633.50 Blue shift	626.15	635.12 Blue shift
B-exciton				606.80		605.69		606.41		606.69
<b>Intensity</b>										
Trion	425.54	782.63	939.08	609.64	621.29	7554.96	3383.10	41,642.54	712.12	12,328.14
A-exciton	955.40	378.21	401.69	136.24	64.85	295.21	658.62	134.53	292.37	145.70
B-exciton				88.73		514.81		300.94		209.37

**Table 2.** The PL peaks positions and intensities of VO<sub>2</sub>/MoS<sub>2</sub>/Si and MoS<sub>2</sub>/Si structures.

On the other hand, trion peak quenching was found in Fig. 6c,d,e; with increasing the Mo-O layer from 120, 180, and 240 s when VO<sub>2</sub> is deposited on MoS<sub>2</sub>/Si structure. We thought that the quenching of PL spectra in Fig. 6c,d,e may be owing to the fact that MoS<sub>2</sub> is an n-type with a close Fermi level to the conduction band. However, the deposited VO<sub>2</sub> layer at thicker Mo-O layer (120, 180, and 240 s) may shift Fermi level to the mid-band gap by drawback the electron coupling of VO<sub>2</sub> and MoS<sub>2</sub><sup>66,67</sup>. Similar results observed using back-gating with SiO<sub>2</sub>/Si<sup>66</sup>, dopants molecule like F4-TCNQ, metal-centered Phthalocyanine molecules on the surface of monolayered TMD<sup>55,68</sup>. It is interesting to note that in all Fig. 6a–e, A-excitons have higher intensities when incorporated VO<sub>2</sub> layer. This result draws high attention for enhancing A-exciton peak intensity and raises strong spin-orbit coupling by incorporating the monoclinic VO<sub>2</sub> thin layer. Moreover, the B-exciton peak was observed in the MoS<sub>2</sub>/Si structure at 606 nm (2.04 eV), but it did not appear in the VO<sub>2</sub>/MoS<sub>2</sub>/Si structure as seen in the insets of Fig. 6b–e. It is known that the PL spectra of MoS<sub>2</sub>, surprisingly, increases with decreasing layer thickness<sup>62</sup>. However, the origin of PL spectrum in MoS<sub>2</sub> arises from the direct excitonic electronic transitions which shows higher radiative recombination rate than nanocrystals<sup>69</sup>. Therefore, the enhanced photoluminescence with increasing the deposition time of Mo-O has to be attributed to a dramatically slower electronic relaxation factor  $\kappa_{relax}$  as in Eq. 1, suggesting a substantial change in electronic structure of MoS<sub>2</sub> when going from the short to longer deposition time of Mo-O as seen in Fig. 6.

$$\eta_{Lum} \sim \frac{\kappa_{rad}}{(\kappa_{rad} + \kappa_{defect} + \kappa_{relax})} \quad (1)$$

where  $\kappa_{rad}$ ,  $\kappa_{defect}$ ,  $\kappa_{relax}$ , and  $\eta_{Lum}$  are representing the rates of radiative recombination, defect trapping, and electron relaxation, Luminescence quantum efficiency within the conduction and valence bands, respectively.

It is concluded that by depositing the VO<sub>2</sub> layer on MoS<sub>2</sub>/Si structure, both trion and exciton peaks get shifted as seen in Table 2. It is implemented that the presence of the VO<sub>2</sub> layer on the surface of the MoS<sub>2</sub>/Si structure results in a redshift through trion peaks, while a blue shift for A-exciton. The peak position of PL for trion is shifted towards lower energy due to the occurred non-radiative electron–hole recombination. However, 30 s sample is out of this rule with a blue and redshift in the trion and A-exciton peak on the VO<sub>2</sub> layer, respectively.

**Surface topography and grain boundary mapping.** AFM has been used to investigate the surface topography, roughness, grain, and grain boundary mapping. Surface topography and parameters such as average roughness R<sub>a</sub>(nm), root mean square or standard deviation of the height value R<sub>q</sub>(nm), height different or peak-to-valley (R<sub>pv</sub>), ten-point height (R<sub>z</sub>), skewness (R<sub>sk</sub>) and kurtosis (R<sub>ku</sub>) as well as fractal and grain analysis were inspected by the XEI software. Figure 7a,d,g,j,m shows a 2D surface topography, Fig. 7b,e,h,k,n shows the 3D visualization, and Fig. 7c,f,l,o shows the grain boundary mapping of the prepared MoWO<sub>3</sub>/VO<sub>2</sub>/MoS<sub>2</sub>/Si thin film with sputtering time of 30, 60, 120, 180, and 240 s, respectively. The films that deposited at short deposition time show higher uniformity, while with increasing the deposition time a small clusters of different sizes less than 100 nm have been observed. The average roughness values of the prepared thin films have summarized in Table 3 and show that 30 s and 180 s thin films have the lowest and highest R<sub>a</sub> value of 3.28 and 48.0 nm, respectively. It seems that with increasing the deposition time of Mo-O, the accumulated nanoparticles show bigger sizes, consequently higher roughness factors. The calculation of the grain and grain boundaries of interfacing thin films are important parameters that provided information about the nature of interfaces between two layers. Figure 7c,f,l,o shows the grain size and grain boundary distribution maps of the prepared thin films. The SEM images of VO<sub>2</sub>, MoO<sub>3</sub>, Mo<sub>0.2</sub>W<sub>0.8</sub>O<sub>3</sub>, and MoS<sub>2</sub>/Si thin films are presented in Figures S1 and S2 and discussed in supplementary information. Large scale MoS<sub>2</sub> thin films have been studied in our previous work by combining CVD and sputtering technique<sup>70</sup>. SEM images (Fig. S2, supplementary information) are provided to illustrate a homogenous and approximately uniform nanoparticles distribution. The SEM images in Fig. S2 (supplementary information) are provided to illustrate the homogeneity and approximate uniform surface distribution of nanoparticles, particularly for sputtering time < 180 s. Also, the AFM images of the MoWO<sub>3</sub>/VO<sub>2</sub>/MoS<sub>2</sub>-Si thin films, Fig. 7, show almost uniformly distributed grains for sputtering time up to 120 s. Besides the presented

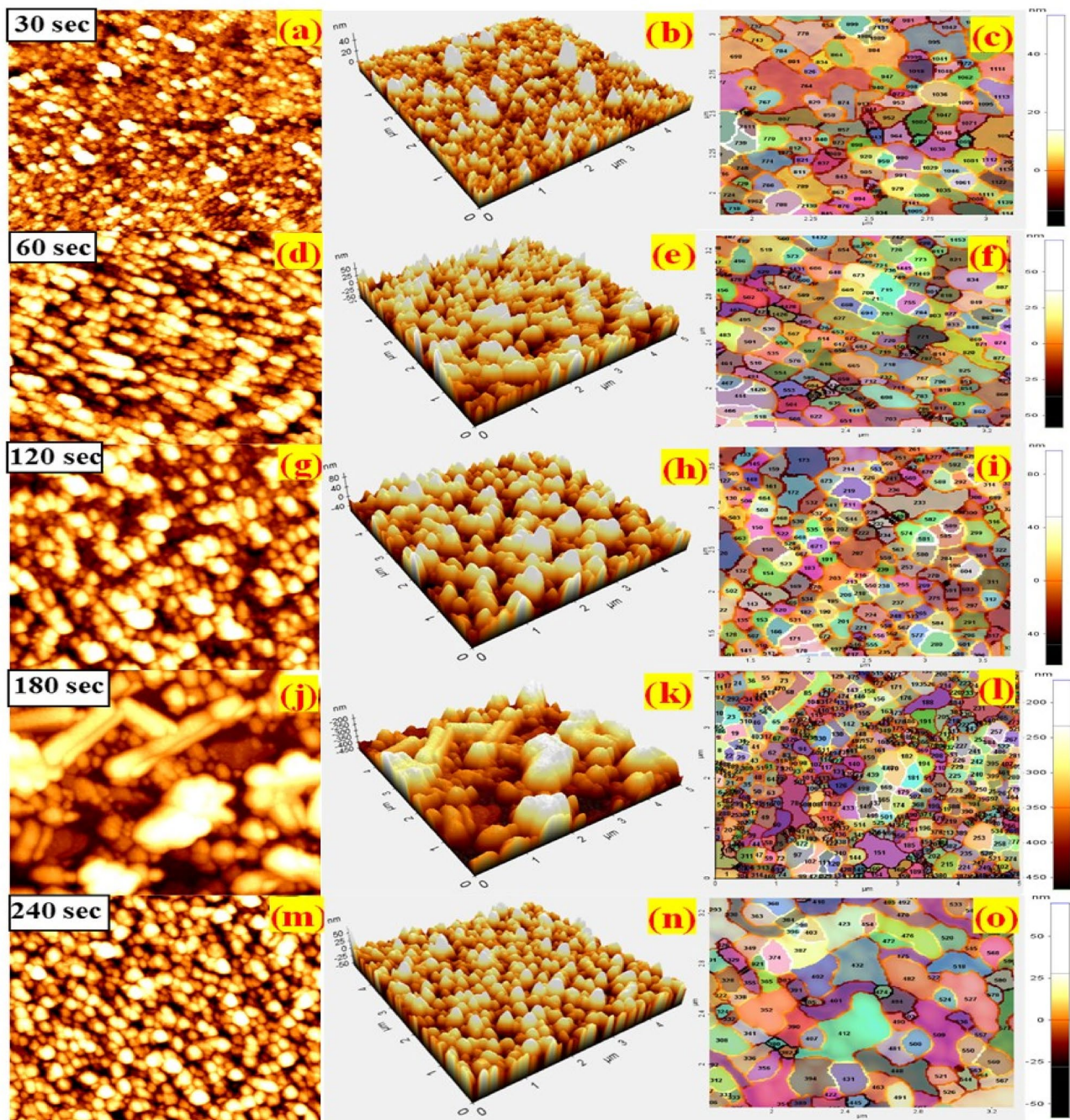


**Figure 7.** 2D AFM images (a, d, g, j, and m), 3D AFM images (b, e, h, k, and n), and the grain/grain boundary mapping (c, f, i, l, and o) of the prepared MoWO<sub>3</sub>/VO<sub>2</sub>/MoS<sub>2</sub>-Si thin film with sputtering time of 30, 60, 120, 180, and 240 s, respectively. XEI software was used for image analysis and processing. [XEI PSIA, Version 1.5, <https://parksystems.com/102-products/park-xe-bio>].

Parameters	30 s	60 s	120 s	180 s	240 s
R <sub>p</sub> (nm)	26.364	76.913	91.878	226.585	73.849
R <sub>q</sub> (nm)	4.458	15.987	22.246	55.048	12.934
R <sub>a</sub> (nm)	3.283	13.460	18.430	48.080	10.688
R <sub>z</sub> (nm)	22.126	59.141	74.573	161.619	48.946
R <sub>sk</sub>	-1.143	0.026	-0.196	-0.172	-0.091
R <sub>ku</sub>	5.362	2.333	2.143	1.973	2.895

**Table 3.** The roughness parameters of MoWO<sub>3</sub>/VO<sub>2</sub>/MoS<sub>2</sub>/Si photodetector.

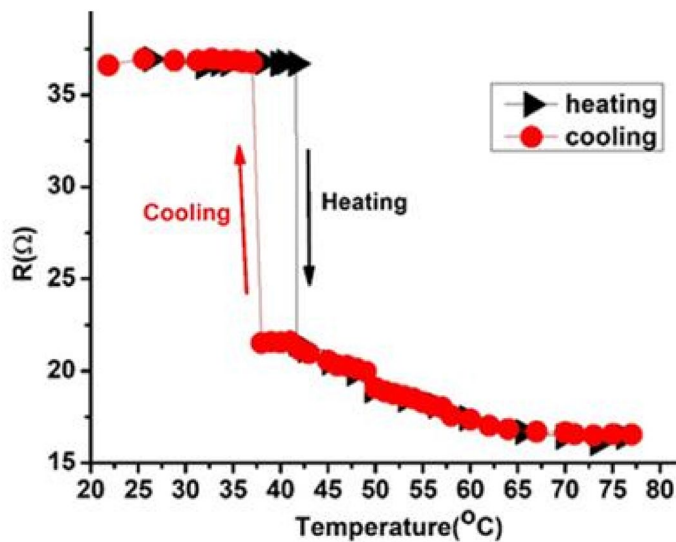


**Figure 8.** Semiconductor–metal phase transition of 50 nm thin VO<sub>2</sub> layer from room temperature to 78 °C.

grain/grain boundaries mapping in Fig. 7, the scanning area of the AFM images was selected to be 5 μm × 5 μm to provide evidence about the ability to scale up the MoS<sub>2</sub> thin films.

**Temperature-resistance measurement (T-R).** The phase transition of the prepared VO<sub>2</sub> thin film has been performed using a four-probe measurement system connected to a heating stage ranging from RT to 78 °C. We investigated the influence of the 50 nm VO<sub>2</sub> thin layer on Raman, PL, and optoelectronic measurements of a few-layers MoS<sub>2</sub> with different sputtering times of Mo-O layer. So, the electrical semiconductor–metal phase change of VO<sub>2</sub> has been tested as depicted in Fig. 8. In our case, the VO<sub>2</sub> phase transition temperature was calculated to be 40 °C by controlling the sputtering condition (high vacuum and long-time annealing temperature) which may affect the lattice-strain and oxygen vacancy concentrations of VO<sub>2</sub><sup>71–73</sup>. The reason for the low semiconductor–metallic phase transition may owing to the high concentration of oxygen vacancies. Oxygen deficient in vanadium oxide (VO<sub>2–δ</sub>) has reported many times to stabilize its metallic state<sup>10</sup>, decrease the semiconductor–metal transition (SMT)<sup>11</sup> and narrowing the bandgap of the monoclinic VO<sub>2</sub> phase<sup>12</sup>. Oxygen vacancies are electron donors with n-type conductivity which can change the electron orbital occupancy and band structures and contribute to the high photocurrent generation when staking by MoS<sub>2</sub><sup>13</sup>. To check these coupling effects between theses layer, UV-optoelectronic measurements have been carried out.

**Electric and optoelectronic properties.** This section discusses the electric characterization of MoS<sub>2</sub>/Si heterostructures before and after depositing the VO<sub>2</sub> layer under dark and UV conditions. In order to investigate the I–V and photoresponse of the prepared devices, we measured the I–V curve under dark and upon UV light illumination by applying a sweep voltage from –5 to +5 V for different sputtering times of Mo-O as shown in Fig. 9. This figure shows the electrical and optoelectronic properties of MoWO<sub>3</sub>/VO<sub>2</sub>/MoS<sub>2</sub>/Si thin film with different thicknesses of the MoS<sub>2</sub> layer. Figure 9a–e shows the current–voltage (I–V) curves under dark and UV illumination at MoS<sub>2</sub> deposition time of 30, 60, 120, 180, and 240 s, respectively. The observed photocurrent in this figure is larger than that reported for previously proposed MoS photodetector with lateral contacts arrangement<sup>31</sup>. The back Al and front Pd-Au contacts may play important rule in that because these contacts allow the vertical electron transport in the heterostructure photodetector besides the lateral electron transportation and consequently 2D conductivity measurements<sup>31,37</sup>. The vertical electron transport offers a high density of active edge sites<sup>37</sup>. Also, our optimized heterojunction photodetector does not have a high-resistance layer like the SiO<sub>2</sub> layer that was previously used and obstruct the vertical electron transport<sup>31</sup>. The back Al contact has been used for better collecting signals. Al metal makes Ohmic contact type with p-Si, which is also observed when probed on two contact pads on the same side, however, noble metals such as Ag, Au, etc. make Schottky contact with p-Si. On the other hand, the Au-Pd front contact was built in the anti-reflection Mo<sub>0.2</sub>W<sub>0.8</sub>O<sub>3</sub> layer, in which the formed Schottky barrier height and width could be controlled by the current passing through the metal–semiconductor contact. Under dark conditions and as predicted by Basyooni et al., a non-linear I–V curve was obtained indicating that a good double-Schottky contact behavior was formed between the front Pd-Au contact and the film surface<sup>34</sup>. The position of asymmetric metal contacts can provide an integrated potential gradient assigned to the work function difference of asymmetric electrodes as previously stated for various applications, such as gas sensors<sup>34</sup> and photodetector<sup>74</sup>, which leads to enhanced device performance as reported here. For instance, Casalino et al. used an asymmetric Al–Si–Cu (metal–semiconductor–metal) structure-based Si photodetector<sup>75</sup>. Moreover, several studies used asymmetric metal contacts for the photodetector application to control the dark current<sup>70,74</sup>.

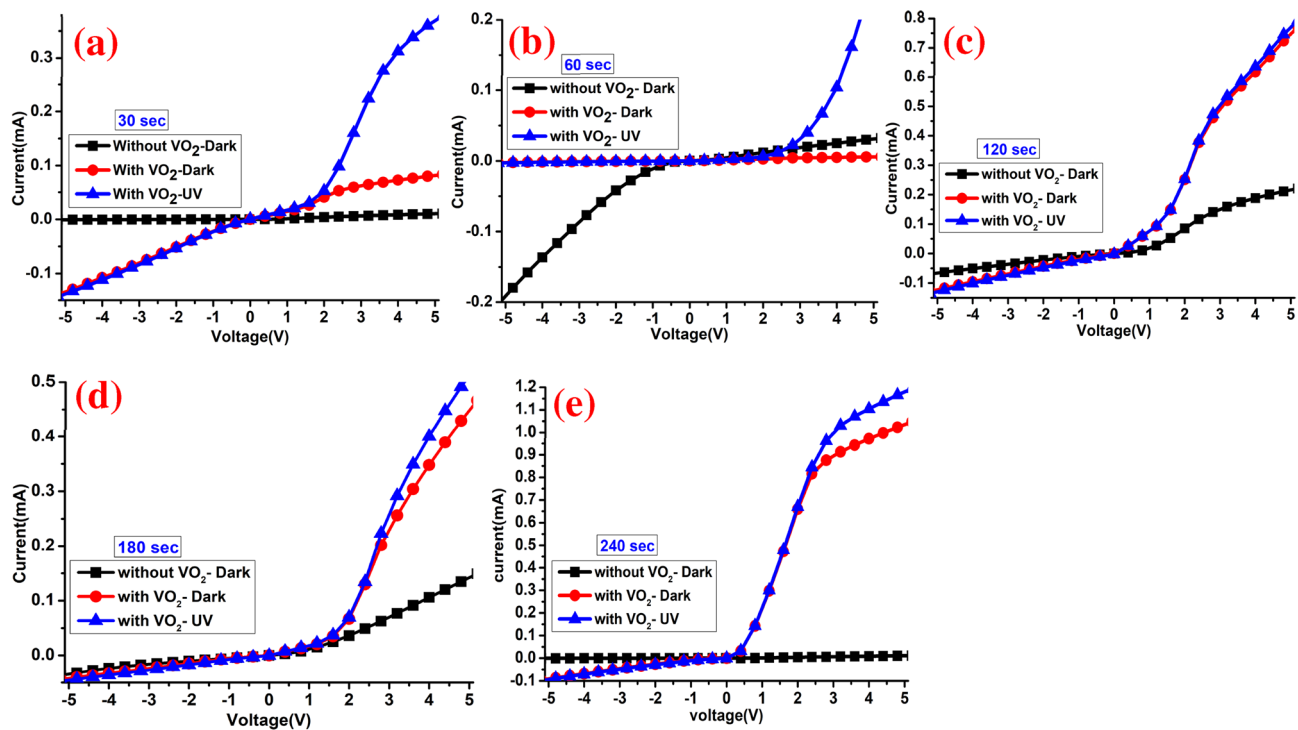
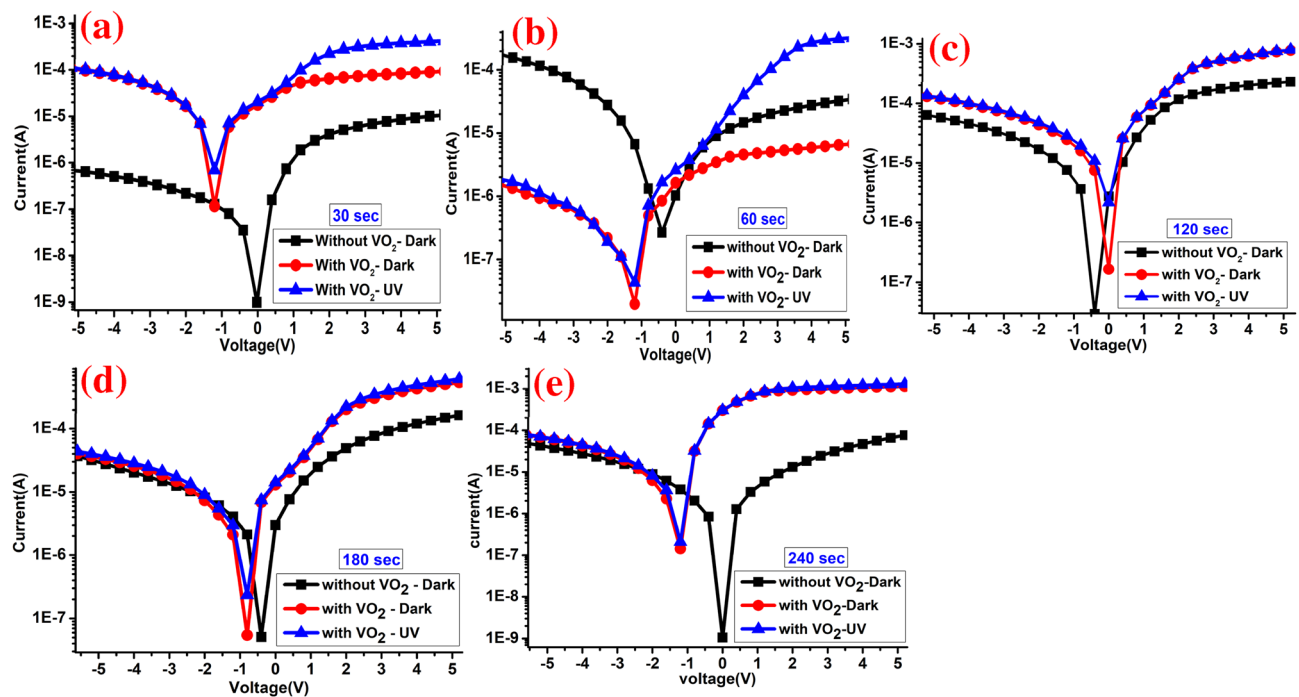


**Figure 9.** The linear I-V characteristics of the  $\text{MoWO}_3/\text{VO}_2/\text{MoS}_2/\text{Si}$  device in dark and under UV illumination with  $\text{MoS}_2$  sputtering time of (a) 30, (b) 60, (c) 120, (d) 180, and (e) 240 s.

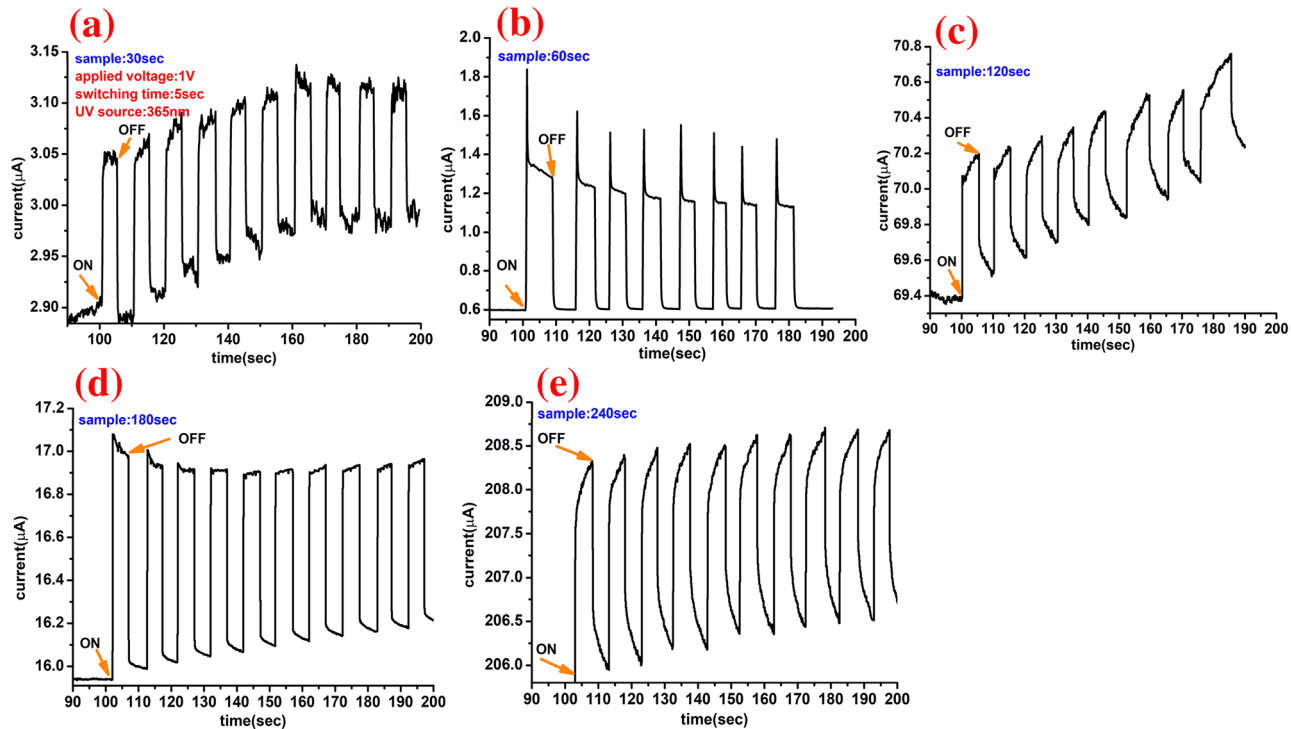
Figure S4 shows the linear and semi-logarithmic scale current–voltage characteristics of  $\text{MoS}_2/\text{Si}$  device without  $\text{VO}_2$  layer under the dark condition with different sputtering times of  $\text{MoS}_2$  layer; 30, 60, 120, 180, and 240 s. The positive part shows an increase in the associated dark current with increasing the sputtering time from 30 to 60 s. While at 120 s, a jump in the forward dark current is observed due to the related folding-effects in  $\text{MoS}_2$ . Folding effect decreases the interlayer coupling and enhances the photoluminescence emission yield of A- and B-exciton peaks as seen in Fig. 5. Whereas instability measurements were observed at the negative bias part. The large increase in the negative dark current for  $\text{MoS}_2$ (60 s) may be attributed to the release of charges that were trapped on  $\text{MoS}_2$ 's surface at the interface trap sites (oxygen sites). The highest reverse dark current, which suggests the lowest potential barrier, was observed at 60 s. This may be ascribed to the values of the optical band gaps as shown in our previous study, whereas the 60 s  $\text{MoS}_2$ -Si thin film displayed optical band gaps of 1.75 and 2.01 eV<sup>33</sup>. By increasing the sputtering time the reverse dark current decreases and almost becomes identical for sputtering time  $\geq 180$  s, as shown in Fig. S4(a,b).

Figure 10a–e shows the log-current curves under dark and UV illumination of 30, 60, 120, 180, and 240 s conditions, respectively. It is clearly seen that UV illumination shifts the logarithmic I–V curve towards the negative voltage region. This behavior may address the induced strain effects from the  $\text{VO}_2$  layer or unidirectional charge transport mechanism from the top to bottom layer due to the different electron concentrations<sup>76</sup>. Interestingly, it seems that the  $\text{VO}_2$  layer enhances the positive and negative current. Meanwhile, the dark current obtained after depositing the  $\text{VO}_2$  layer on the surface of  $\text{MoS}_2/\text{Si}$  is about 2–3 folds' improvement over pure  $\text{MoS}_2/\text{Si}$  device for 30 and 60 s samples, as in Fig. 10a,b. The observed higher value of photocurrent under UV illumination is also attributed to enhancement though the band-to-band excitation in the  $\text{VO}_2/\text{MoS}_2/\text{Si}$  region. Moreover, carrier recombination and tunneling across the device junction may be addressed as a reason for the enhancement I–V under UV illumination. Nevertheless, fast response and recovery times, high responsivity, high reliability, and low signal-to-noise ratio are important characteristics for detector applications<sup>77,78</sup>, which is discussed below in detail.

**Transient response.** Figure 11a–e shows the ON-OFF time-resolved photoresponses of  $\text{MoWO}_3/\text{VO}_2/\text{MoS}_2/\text{Si}$  devices with varying  $\text{MoS}_2$  sputtering time (30, 60, 120, 180, and 240 s) in dark and under UV illumination. These optoelectronic transient/dynamic curves were measured with a switching time of 5 s, a bias voltage of 1 V, and UV illumination of 365 nm. Also, the optical modulations (photocurrent-time characteristics@ 1 V) under dark and UV illuminations of  $\text{Mo}_{0.2}\text{W}_{0.8}\text{O}_3/\text{VO}_2/\text{MoS}_2/\text{Si}$  devices are presented in Figure S5 (supplementary information). Note that the ON/OFF and OFF/ON transitions of the UV light source are repeated many times for each 5 s at a bias voltage of 1 V. The time-resolved photoresponse curves in Fig. 11 show different sputtering time dependence. The curves at 30 and 120 s show increasing on/off behaviors, whereas the curves at 60, 180, and 240 s show stable on/off behaviors. The increasing on/off behaviors in Fig. 11a,c may come from some organic trap states that accumulated during the CVD sulfurization process. While, the stable on/off behaviors in Fig. 11b,d,e can be attributed to the high stability, high quality, and low density of the defects.



**Figure 10.** The semi-logarithmic scale I-V of  $\text{MoWO}_3/\text{VO}_2/\text{MoS}_2/\text{Si}$  device under dark and UV illumination with  $\text{MoS}_2$  sputtering time of (a) 30, (b) 60, (c) 120, (d) 180, and (e) 240 s.



**Figure 11.** ON/OFF time-resolved photoresponse of the  $\text{MoWO}_3/\text{VO}_2/\text{MoS}_2/\text{Si}$  device with  $\text{MoS}_2$  sputtering time of (a) 30, (b) 60, (c) 120, (d) 180, and (e) 240 s. All measurements were carried out at a bias voltage of 1 V, UV illumination of 365 nm, and switching time of 5 s.

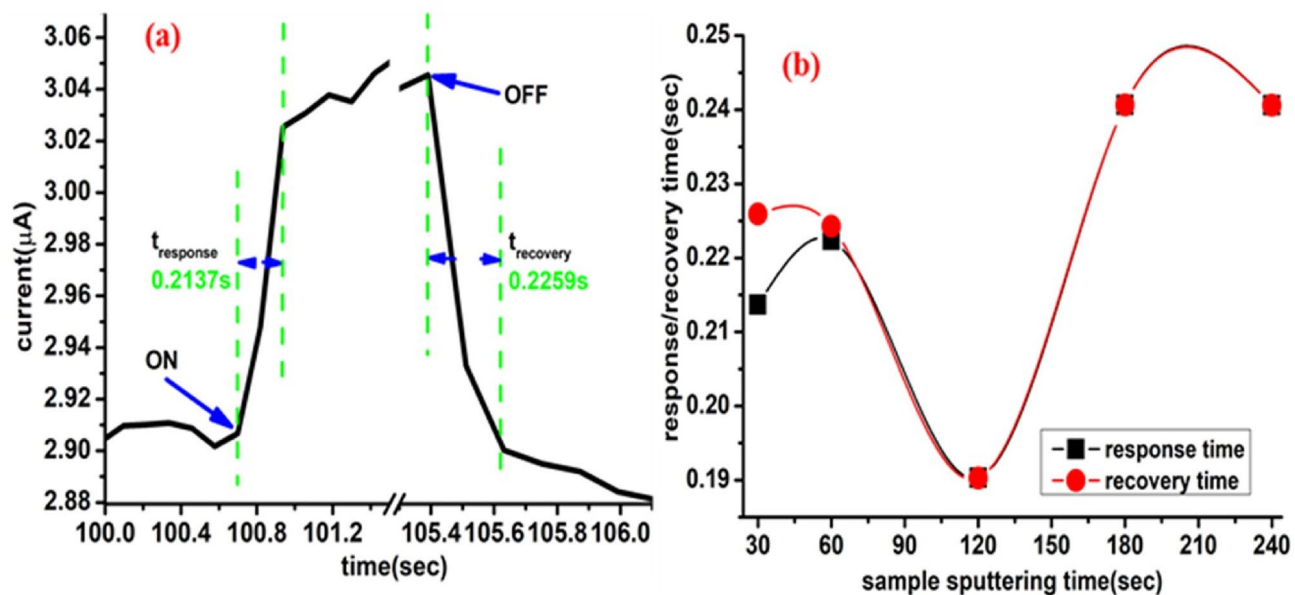


**Figure 12.** (a) Enlarged view of a single current–time photoresponse cycle for  $\text{MoWO}_3/\text{VO}_2/\text{MoS}_2$  (30 s)/Si UV photodetector to identify the response and recovery times and (b) the estimated response and recovery times as a function of the sputtering time.

The response/raise time was measured when the light source turned on, while the recovery/decay time was measured when the light turned off as shown in Fig. 12a. The response and recovery times have been estimated from the ON/OFF dynamic photoresponses at different sputtering times, Fig. 11. The combined sputtering and CVD deposition process of  $\text{MoWO}_3/\text{VO}_2/\text{MoS}_2/\text{Si}$  UV photodetector device shows symmetrical response and recovery time which not exceed 0.25 s using the selected wavelength (365 nm) and bias (1 V), as shown in Fig. 12b. Consequently, our proposed photodetector is considered more efficient than the previously tested photodetector by Ang et al.<sup>78</sup>.

The fast response and recovery speed, indicating that electron–hole pairs could be effectively generated and separated in the proposed structure under UV illumination at room temperature. It is important to note that the fabricated device using  $\text{MoS}_2$ (120 s) shows the fastest response/recovery times (0.19 s at 1 V) among the studied devices as shown in Fig. 12b. The fast response/recovery time at 120 s can indicate the fast and stable generation and separation of the electron–hole pairs. Unlike Dhyani and Das who reported rapid response for the silicon- $\text{MoS}_2$  photodetector@ 580 nm and 3 V bias<sup>79</sup>, our measurements are performed without any external series resistance. Nevertheless, it is known that higher applied bias voltage can generate more photocurrent and consequently decrease the response and recovery time. A clear high photocurrent can be observed in the ON state at 1 V which makes the gate voltage lowers the potential barriers at the contacts, resulting in highly efficient photogenerated carrier extraction and thus increased photocurrent at a low applied voltage (1 V). The reason behind this is that the gate voltage can affect the height of the Schottky barrier between the metal contact and film surface and thus shift the Fermi level<sup>80,81</sup>. It seems that our designed photodetector did not require high bias voltage which makes it more applicable for low power photodetector technology.

**Photocurrent gain ( $P_g$ ) and photoresponsivity ( $R_s$ ).** The induced photocurrent  $I_{ph}$  is given by  $I_{ph} = I_{Light} - I_{Dark}$ , where  $I_{ph}$  increases with increasing the applied voltage and the light power<sup>82</sup>. Photocurrent gain ( $P_g$ ) can be defined and determined by  $P_g = (I_{photo} - I_{dark})/I_{dark}$ , where  $I_{photo}$  and  $I_{dark}$  are photocurrent and dark current respectively<sup>77</sup>.

Also, the detector responsivity ( $R_s$ ) can be expressed as  $R_s = \Delta I/(A \times P)$ , where  $\Delta I$  is the difference between the photocurrent and dark current,  $A$  is the illuminated area, and  $P$  is the UV light power. Figure 13a shows the photocurrent and photocurrent gain of the tested samples under a 365 nm UV illumination source. Figure 13b demonstrates the responsivity in A/W of  $\text{MoS}_2/\text{Si}$  and  $\text{MoWO}_3/\text{VO}_2/\text{MoS}_2/\text{Si}$  photodetectors with different  $\text{MoS}_2$  sputtering time (30–240 s). In both photodetectors, the responsivity values reflect nearly linear increases by increasing the sputtering time to 180 s.  $\text{MoWO}_3/\text{VO}_2/\text{MoS}_2/\text{Si}$  UV detector responsivity shows high values ranging from 0.3 to 4.7 A/W, which corresponds to 30 to 180 s  $\text{MoS}_2$  sputtering time. The optimized value at 180 s is higher than that reported by Li et al. (2.4 mW cm<sup>-2</sup>)<sup>83</sup>. The enhanced photoresponsivity by interfacing the  $\text{VO}_2$  layer may be owing to the film strain include stresses arising from the different thermal expansion coefficients of the  $\text{VO}_2$  and  $\text{MoS}_2/\text{Si}$  film due to a high deposition/sulphurization temperatures of ~ 400/650 °C and growth stresses arising from crystal structure changes after deposition. Nevertheless, more efficient light absorption involving more  $e-h$  pairs generation, resulting in higher mobility and more detection capability.

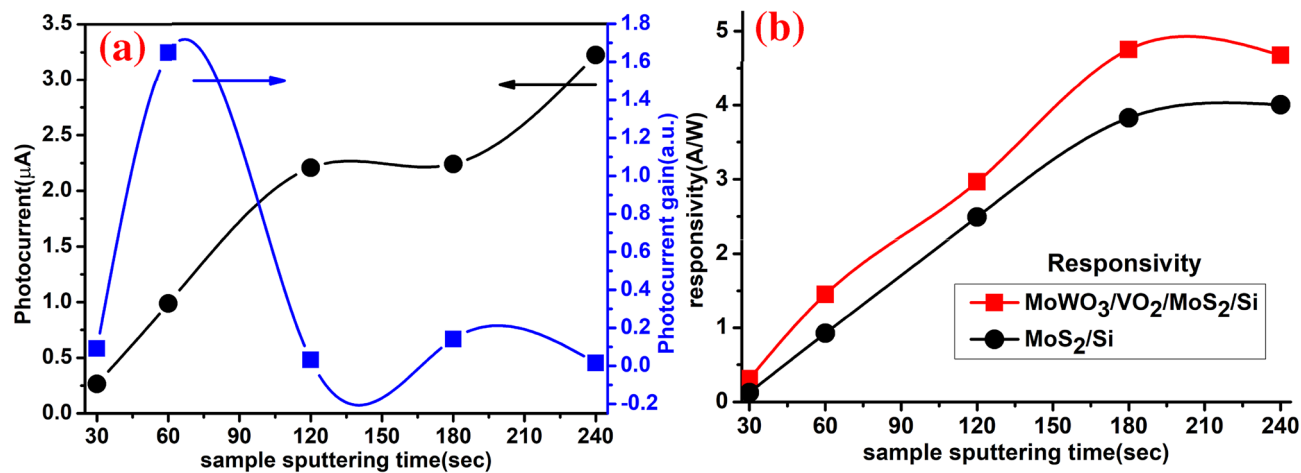


**Figure 13.** (a) the photocurrent and photocurrent gain of MoWO<sub>3</sub>/VO<sub>2</sub>/MoS<sub>2</sub>/Si photodetector and (b) responsivity for both MoS<sub>2</sub>/Si and MoWO<sub>3</sub>/VO<sub>2</sub>/MoS<sub>2</sub>/Si photodetectors as a function of the MoS<sub>2</sub> sputtering time.

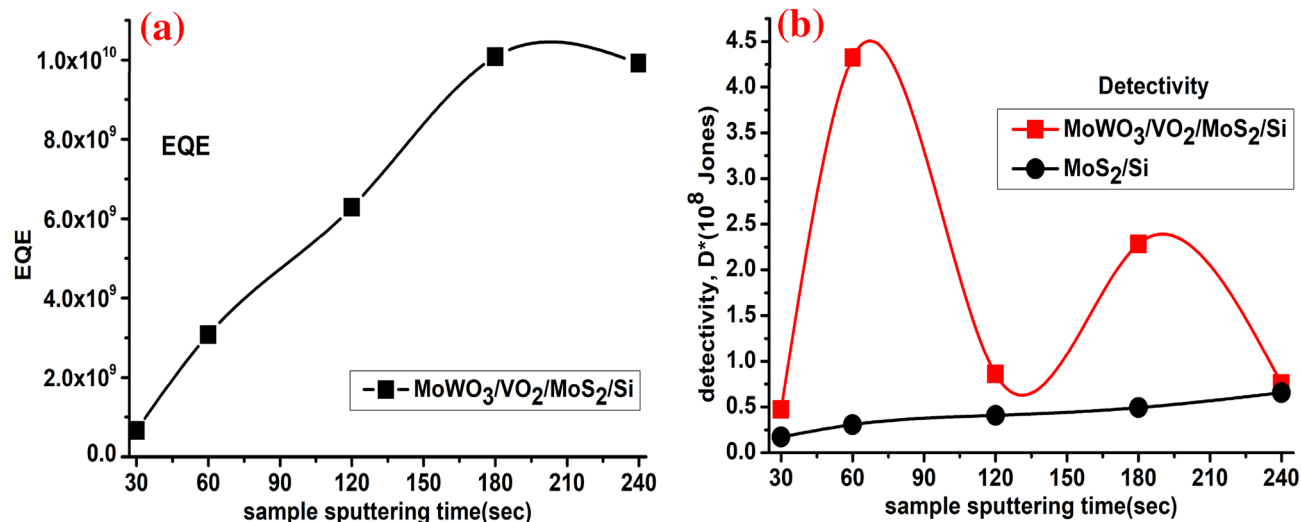


**Figure 14.** (a) The EQE of MoWO<sub>3</sub>/VO<sub>2</sub>/MoS<sub>2</sub>/Si photodetector as a function of the MoS<sub>2</sub> sputtering time and (b) the detectivity of both MoS<sub>2</sub>/Si and MoWO<sub>3</sub>/VO<sub>2</sub>/MoS<sub>2</sub>/Si photodetectors as a function of the MoS<sub>2</sub> sputtering time.

**External quantum efficiency (EQE) and detectivity (D\*).** In order to produce the photocurrent  $I_{ph}$ , the fraction of the extracted free charge carriers to the photo flux  $\phi_{in}$  collected at a given energy  $E_{ph}$  is called the External Quantum Efficiency, defined by<sup>84</sup> as  $EQE = \frac{hcR_\lambda}{e\lambda}$ , where  $h$  is the Planck's constant ( $\sim 4.135 \times 10^{-15}$  eV s),  $e$  is the elementary electron charge ( $\sim 1.602 \times 10^{-9}$  C),  $c$  is the light velocity ( $\sim 3 \times 10^8$  m/s), and  $\lambda$  is the excitation wavelength (365 nm). The EQE values as a function of the prepared samples are plotted in Fig. 14a, where EQE varies from  $6.6 \times 10^8$  to  $\sim 1.0 \times 10^{10}$  at 365 nm which considered higher than the mesoscopic multilayer MoS<sub>2</sub> as reported before<sup>85</sup>. Another important figure of merit of a photodetector is the detectable signal<sup>82</sup>, referred by the specific detectivity measured in Jones, which given by  $D^* = \frac{(AB)^{0.5} R_\lambda}{i_n} (\text{cmHz}^{\frac{1}{2}} \text{W}^{-1})$ , where  $A$  is the effective area of the d in cm<sup>2</sup>,  $B$  is the bandwidth, and  $i_n$  is the measured noise current. If the shot noise from the dark current is the main noise source, the specific detectivity can be simplified as  $D^* = \frac{R_\lambda A^{0.5}}{(2eI_{dark})^{0.5}}$ , Where  $e$  is the charge of an elementary electron<sup>86</sup>. The calculated D\* for MoS<sub>2</sub>/Si and MoWO<sub>3</sub>/VO<sub>2</sub>/MoS<sub>2</sub>/Si is depicted in Fig. 14b. D\* of MoS<sub>2</sub>/Si device shows a progressive increase with sputtering time from 30 to 240 s. For MoS<sub>2</sub>/Si device, the maximum D\* was  $0.4 \times 10^8$  Jones. While the maximum D\* for the MoWO<sub>3</sub>/VO<sub>2</sub>/(60 s)MoS<sub>2</sub>/Si is  $\sim 4.3 \times 10^8$  Jones at RT and applied voltage of 1 V. In contrast the MoWO<sub>3</sub>/VO<sub>2</sub>/MoS<sub>2</sub>/Si with a 30 s deposition time shows D\* of  $0.47 \times 10^8$  Jones.

**Mechanism.** Now we turn to the underlying photoresponse mechanism of the VO<sub>2</sub>/MoS<sub>2</sub>/Si as a UV photodetector device. The photoresponse properties of VO<sub>2</sub>/MoS<sub>2</sub>/Si heterojunction can be understood from the

energy-band alignment diagram as in Fig. 1b. Due to the free dangling bonds of the surfaces of MoS<sub>2</sub> film, the MoS<sub>2</sub>/Si heterojunction can be affected by lattice matching. Clearly, the implanting of VO<sub>2</sub> layer-based UV photodetector was overwhelmingly play an important role in enhancing the Raman signal/intensity, PL intensity, electrical and optoelectronic performance of MoS<sub>2</sub>/Si device. Under the zero-bias condition, an insignificant current was observed due to the high depletion layer at the n-p (MoS<sub>2</sub>-Si) junction which restricts the movement of the carriers. Under VO<sub>2</sub> interfacing, both positive and negative current increased significantly and the photocurrent I<sub>ph</sub> of VO<sub>2</sub>/MoS<sub>2</sub>/Si film is much higher than that in MoS<sub>2</sub>-Si, which can be attributed to the more photon absorption on the top of MoWO<sub>3</sub>/VO<sub>2</sub> layer and larger photocurrent-gain due to higher carrier mobility<sup>87,88</sup>. With increasing the amount of Mo-O (deposition time of 30, 60, 120, 180, and 240 s), the induced current is enhanced due to the more electron-hole pair generation by UV light absorption and the applied voltage shifts dramatically towards negative voltage, which indicates the continuous accumulation of electrons in the vertical VO<sub>2</sub>-MoS<sub>2</sub> channel as seen from the logarithmic scale current. In the positive voltage region, the MoS<sub>2</sub>/Si n-p structure shows that umpteen electrons are accumulated on the MoS<sub>2</sub> band which shifts Fermi level near the conduction band. Because 1 V is able to decrease the depletion width and the barrier height, electrons are able to overcome the barrier height through thermionic emission, resulting in a high flux of photocurrent and more efficient photocurrent extraction. It is interesting to observe that under a shorter sputtering time of Mo-O (30, then 60 s), a significant forward photocurrent was observed which did not observe before in MoS<sub>2</sub>/Si structures<sup>52,89</sup>. Meanwhile, with increasing the Mo-O content, MoO<sub>3</sub> starts to get folded and the reverse photocurrent starts to get highlighted as seen in the semi-logarithmic scale I-V, Fig. 10.

## Conclusion

In summary, the next generation of optoelectronic devices integrates the physics of light-matter interaction of 2D materials at nanoscale for light-harvesting applications and these optoelectronic devices can control the light that converts trions, excitons, and photons to electrical signals. Our approach is based on a high vacuum deposition of Mo-O compound at 400 °C, followed by a sulphurization process in a chemical vapor deposition tube. Here we study the interfacing effect of monoclinic VO<sub>2</sub> with MoS<sub>2</sub> film for UV optoelectronic applications. It showed that different thicknesses of the MoS<sub>2</sub> compound have a direct effect on the Raman, PL, electrical, optoelectronics of MoS<sub>2</sub> peaks. A redshift was observed in Raman spectra with a high electronic coupling between VO<sub>2</sub> and MoS<sub>2</sub> for the case of 180 s sputtering time. Photoluminescence measurements showed that the intensity of the trion peak has a higher intensity than the A-exciton peak for MoS<sub>2</sub>/Si structure. On the other hand, the opposite case was observed for the VO<sub>2</sub>/MoS<sub>2</sub>/Si device. Current-voltage, response/recovery time, external quantum efficiency, time-resolved photocurrent, and detectivity, photocurrent gain, photo-responsivity of VO<sub>2</sub>/MoS<sub>2</sub>/Si device have been demonstrated. It's shown that the increase of the deposition time of MoS<sub>2</sub> from 30 to 240 s enhances the photo-absorption, photo-responsivity, and external quantum efficiency of the MoWO<sub>3</sub>/VO<sub>2</sub>/MoS<sub>2</sub>/Si device due to the associated folding effects of MoO<sub>3</sub>. These results show a multiplexed photodetector fabrication technique of high reproducible and scalable process based on CVD and PVD system and draw high attention towards the interfacing effects of strongly correlated oxide films MoS<sub>2</sub> devices.

## Materials and methods

**Device fabrication.** Preparation of MoS<sub>2</sub> layer on p-type Si substrate has prepared through two steps in physical vapor deposition (PVD)—Radio Frequency magnetron sputtering system, followed by chemical vapor deposition (CVD) process. Si substrates were cleaned through many steps; firstly, kept in NH<sub>4</sub>OH-H<sub>2</sub>O<sub>2</sub> solution diluted with de-ionized (DI) water for 5 min at 75 °C, then rinsed with DI water for 5 min. After that, they left in HF (%5) solution for 5 s, then rinsed in DI water and dried with high purity N<sub>2</sub>. Immediately, the cleaned Si-substrates transferred to a  $3 \times 10^{-7}$  Torr RF magnetron sputtering system (VAKSIS Midas 3M1T). In-situ Ar-plasma source has activated for 10 min at a power of 100 W and low pressure of  $6 \times 10^{-3}$  Torr at room temperature to activate the Si surface. Mo-O thin films were grown using a 3-inch. pure molybdenum target (99.9%) utilizing Ar plasma as a carrier gas and O<sub>2</sub> as a reactive gas. The substrate temperature was stabilized at 400 °C for more than 30 min before the deposition process with steps of 100 °C/30 min. The O<sub>2</sub> and Ar flow rates were kept constant, whereas O<sub>2</sub>/(Ar + O<sub>2</sub>) of ¼ ratio. The deposition was carried out at  $5 \times 10^{-3}$  Torr and 137 W with different sputtering times of 30, 60, 120, 180, and 240 s. The system was kept to cool down normal up to the room temperature (RT), then immediately transferred to the two-zone CVD quartz chamber (MTI-OTF 1200 system) for the sulphurization process. The as-deposited molybdenum oxide (Mo-O) thin films transferred to the center of the CVD furnace and the temperature is raised to 650 °C. Sulphur powder (0.5 g) is put in a ceramic boot with 100sccm high purity Ar source. An external heating belt with a distance of 50 cm to the substrate was used to evaporate the sulphur for 22 min. Then, the system cooled down until RT with the same flow rate of Ar (100 sccm).

After forming the MoS<sub>2</sub> layer, a thin layer of monoclinic VO<sub>2</sub> has grown. The same sputtering system was used with a 190 W deposition power and Ar/O<sub>2</sub> ratio was 41/2.2 sccm, while the deposition time was set to produce 50 nm film thickness. Then the samples were in-situ annealed at 400 °C for 2 h with 50 sccm Ar flow. A protective and anti-reflection thin layer of Mo<sub>0.2</sub>W<sub>0.8</sub>O<sub>3</sub> was deposited on the surface of VO<sub>2</sub> as optimized in our previous work<sup>34</sup>. High vacuum thermal evaporation system was used to deposit aluminum and gold-palladium that used as a back and front contacts, respectively.

**Device characterization.** The crystal structures were analyzed using Grazing Incidence X-ray diffraction (XRD GNR ADP PRO 2000), with CuK $\alpha$  ( $\lambda = 1.5405$  Å) radiation source with a step of 0.01. VO<sub>2</sub> layer was deposited at a high vacuum condition to ensure its high crystallinity and low semiconductor-metallic phase transition. Parameters such as space group, diffraction peaks, angles, Wyckoff position of vanadium (V) and

oxygen (O) atoms, ratio of O:V, and oxygen vacancy concentrations were calculated from refinement analysis. The refinement calculations were done using Match and Fullprof Suite program. Moreover, the refined structures were plotted in a three-dimensional view using 3D visualization VESTA program. The surface morphology was recorded using scanning electron microscopy (SEM) TESCANMAIA3 XMU. Atomic Force Microscopy (AFM) has been used to investigate the surface topography, roughness, and grain mapping. Each sample was characterized by XE-6 AFM (Park Systems Corp., Suwon-Korea) that controlled with XEP software for data acquisition and XEI software for image analysis and processing. AFM images were obtained through a  $0.5 \times 0.5 \mu\text{m}$  area (x-y accessible area) at a 0.5 Hz scan rate. Measurements were taken with a non-contact mode using a PPP-NCHR silicon cantilever consisting of tip radius  $< 10 \text{ nm}$  and 42 N/m force constant (Nanosensors TM, Neuchâtel-Switzerland). Raman measurements and photoluminescence (PL) spectra were carried out using Renishaw in Via Confocal Raman microscope with a 532 nm laser beam, while an incident laser power of 3 mW was chosen to acquire a single Raman spectrum. The temperature-resistance measurement of monoclinic and high crystalline nanostructure VO<sub>2</sub> thin film has been performed using a four-probe measurement system connected to a heating stage ranging from RT to 100 °C. The electrical and optoelectronics measurements were measured using 2450 Kethley Source -Meter and 365 nm ultraviolet (UV) light lamp for optoelectronic measurements.

Received: 26 May 2020; Accepted: 9 September 2020

Published online: 28 September 2020

## References

1. Kim, J. K. *et al.* Trap-mediated electronic transport properties of gate-tunable pentacene/MoS<sub>2</sub> p-n heterojunction diodes. *Sci. Rep.* **6**, 36775 (2016).
2. Yu, J., Li, J., Zhang, W. & Chang, H. Synthesis of high quality two-dimensional materials via chemical vapor deposition. *Chem. Sci.* **6**, 6705–6716 (2015).
3. Cai, Z., Liu, B., Zou, X. & Cheng, H. M. Chemical vapor deposition growth and applications of two-dimensional materials and their heterostructures. *Chem. Rev.* **118**, 6091–6133 (2018).
4. Wang H *et al.* (2012) Large-scale 2D electronics based on single-layer MoS<sub>2</sub> grown by chemical vapor deposition. In *Technical digest—international electron devices meeting, IEDM* (2012). <https://doi.org/10.1109/IEDM.2012.6478980>.
5. Sharma, D. *et al.* Transfer characteristics and low-frequency noise in single- and multi-layer MoS<sub>2</sub> field-effect transistors. *Appl. Phys. Lett.* **107**, 162102 (2015).
6. Nicolosi, V., Chhowalla, M., Kanatzidis, M. G., Strano, M. S. & Coleman, J. N. Liquid exfoliation of layered materials. *Science* **340**, 1226419 (2013).
7. Coleman, J. N. *et al.* ChemInform abstract: two-dimensional nanosheets produced by liquid exfoliation of layered materials. *ChemInform* **42**, 568 (2011).
8. Yu, X., Prévot, M. S. & Sivula, K. Multiflake thin film electronic devices of solution processed 2D MoS<sub>2</sub> enabled by sonopolymer assisted exfoliation and surface modification. *Chem. Mater.* **26**, 5892–5899 (2014).
9. Paton, K. R. *et al.* Scalable production of large quantities of defect-free few-layer graphene by shear exfoliation in liquids. *Nat. Mater.* **13**, 624–630 (2014).
10. Varrla, E. *et al.* Large-scale production of size-controlled MoS<sub>2</sub> nanosheets by shear exfoliation. *Chem. Mater.* **27**, 1129–1139 (2015).
11. Knirsch, K. C. *et al.* Basal-plane functionalization of chemically exfoliated molybdenum disulfide by diazonium salts. *ACS Nano* **9**, 6018–6030 (2015).
12. Eda, G. *et al.* Photoluminescence from chemically exfoliated MoS<sub>2</sub>. *Nano Lett.* **11**, 5111–5116 (2011).
13. Yang, X. Y. & Chauhan, N. *Photoenergy and Thin Film Materials*. Wiley, New York. <https://doi.org/10.1002/9781119580546> (2019).
14. Giannazzo, F., Lara Avila, S., Eriksson, J. & Sonde, S. *Integration of 2D Materials for Electronics Applications* (MDPI, Basel, 2019).
15. Browning, R. *et al.* Atomic layer deposition of MoS<sub>2</sub> thin films. *Mater. Res. Exp.* **2**, 035006 (2015).
16. Loh, T. A. J. & Chua, D. H. C. Growth mechanism of pulsed laser fabricated few-layer MoS<sub>2</sub> on metal substrates. *ACS Appl. Mater. Interfaces* **6**, 15966–15971 (2014).
17. Serrao, C. R. *et al.* Highly crystalline MoS<sub>2</sub> thin films grown by pulsed laser deposition. *Appl. Phys. Lett.* **106**, 052101 (2015).
18. Ma, X. & Shi, M. Thermal evaporation deposition of few-layer MoS<sub>2</sub> films. *Nano-Micro Lett.* **5**, 135–139 (2013).
19. Wu, S. *et al.* Vapor-solid growth of high optical quality MoS<sub>2</sub> monolayers with near-unity valley polarization. *ACS Nano* **7**, 2768–2772 (2013).
20. Pacley, S. *et al.* Impact of reduced graphene oxide on MoS<sub>2</sub> grown by sulfurization of sputtered MoO<sub>3</sub> and Mo precursor films. *J. Vac. Sci. Technol. A Vac. Surf. Films* **34**, 041505 (2016).
21. Hussain, S. *et al.* Synthesis and characterization of large-area and continuous MoS<sub>2</sub> atomic layers by RF magnetron sputtering. *Nanoscale* **8**, 4340–4347 (2016).
22. Matsura, K. *et al.* Low-carrier-density sputtered MoS<sub>2</sub> film by vapor-phase sulfurization. *J. Electron. Mater.* **47**, 3497–3501 (2018).
23. Imai, Y., Solovyev, I. & Imada, M. Electronic structure of strongly correlated systems emerging from combining path-integral renormalization group with the density-functional approach. *Phys. Rev. Lett.* **95**, 176405 (2005).
24. Sass, B. *et al.* Structural and electronic properties of epitaxial V<sub>2</sub>O<sub>3</sub> thin films. *J. Phys. Condens. Matter* **16**(1), 77–87 (2004).
25. Rozenberg, M. J. *et al.* Optical conductivity in Mott-Hubbard systems. *Phys. Rev. Lett.* **75**, 105–108 (1995).
26. Tongay, S. *et al.* Tuning interlayer coupling in large-area heterostructures with CVD-grown MoS<sub>2</sub> and WS<sub>2</sub> monolayers. *Nano Lett.* **14**, 3185–3190 (2014).
27. Sun, Y. *et al.* Probing local strain at MX<sub>2</sub>-Metal boundaries with surface plasmon-enhanced Raman scattering. *Nano Lett.* **14**, 5329–5334 (2014).
28. Goodenough, J. B. The two components of the crystallographic transition in VO<sub>2</sub>. *J. Solid State Chem.* **3**, 490–500 (1971).
29. Budai, J. D. *et al.* In situ X-ray microdiffraction studies inside individual VO<sub>2</sub> microcrystals. *Acta Mater.* **61**, 2751–2762 (2013).
30. McWhan, D. B., Marezio, M., Remeika, J. P. & Dernier, P. D. X-ray diffraction study of metallic VO<sub>2</sub>. *Phys. Rev. B* **10**, 490–495 (1974).
31. Oliva, N. *et al.* Van der Waals MoS<sub>2</sub>/VO<sub>2</sub> heterostructure junction with tunable rectifier behavior and efficient photoresponse. *Sci. Rep.* **7**, 14250 (2017).
32. Lin, Y. C. *et al.* Photoluminescence of monolayer transition metal dichalcogenides integrated with VO<sub>2</sub>. *J. Phys. Condens. Matter* **28**, 504001 (2016).

33. Karataş, A. & Yilmaz, M. Molybdenum disulfide thin films fabrication from multi-phase molybdenum oxide using magnetron sputtering and CVD systems together. *Superlattices Microstruct.* **143**, 106555 (2020).
34. Basyooni, M. A., Zaki, S. E., Ertugrul, S., Yilmaz, M. & Eker, Y. R. Fast response of CO<sub>2</sub> room temperature gas sensor based on mixed-valence phases in molybdenum and tungsten oxide nanostructured thin films. *Ceram. Int.* **46**, 9839–9853. <https://doi.org/10.1016/j.ceramint.2019.12.259> (2020).
35. US7196314B2—Image sensor and pixel having an anti-reflective coating over the photodiode—Google Patents. <https://patents.google.com/patent/US7196314B2/en>. Accessed on 18th June 2020.
36. US8546742B2—Array of nanowires in a single cavity with anti-reflective coating on substrate—Google Patents. <https://patents.google.com/patent/US8546742B2/en>. Accessed on 2nd July 2020.
37. US6803249B2—Method of making an integrated photodetector in which a silicon nitride layer forms an anti-reflective film and part of multi-layer insulator within transistor structures—Google Patents. <https://patents.google.com/patent/US6803249B2/en>. Accessed on 2nd July 2020.
38. Zhang, J. *et al.* Evolution of structural and electrical properties of oxygen-deficient VO<sub>2</sub> under low temperature heating process. *ACS Appl. Mater. Interfaces* **9**, 27135–27141 (2017).
39. Wang, X., Wang, Z., Zhang, G. & Jiang, J. Insight into electronic and structural reorganizations for defect-induced VO<sub>2</sub> metal-insulator transition. *J. Phys. Chem. Lett.* **8**, 3129–3132 (2017).
40. Chen, L. *et al.* First-principles study of the effect of oxygen vacancy and strain on the phase transition temperature of VO<sub>2</sub>. *RSC Adv.* **6**, 86872–86879 (2016).
41. Fan, S., Fan, L., Li, Q., Liu, J. & Ye, B. The identification of defect structures for oxygen pressure dependent VO<sub>2</sub> crystal films. *Appl. Surf. Sci.* **321**, 464–468 (2014).
42. Yuan, Z., Hou, J. & Liu, K. Interfacing 2D semiconductors with functional oxides: fundamentals, properties, and applications. *Crystals* **7**, 265 (2017).
43. Zhang, X. *et al.* Phonon and Raman scattering of two-dimensional transition metal dichalcogenides from monolayer, multilayer to bulk material. *Chem. Soc. Rev.* **44**, 2757–2785 (2015).
44. Hui, Y. Y. *et al.* Exceptional tunability of band energy in a compressively strained trilayer MoS<sub>2</sub> sheet. *ACS Nano* **7**, 7126–7131 (2013).
45. Manzeli, S., Allain, A., Ghadimi, A. & Kis, A. Piezoresistivity and strain-induced band gap tuning in atomically thin MoS<sub>2</sub>. *Nano Lett.* **15**, 5330–5335 (2015).
46. Kotula, A. P., Snyder, C. R. & Migler, K. B. Determining conformational order and crystallinity in polycaprolactone via Raman spectroscopy. *Polymer (Guildf)* **117**, 1–10 (2017).
47. Nikolaeva, G. Y. *et al.* Using Raman spectroscopy to determine the structure of copolymers and polymer blends. *J. Phys. Conf. Ser.* **826**, 012002 (2017).
48. Samuel, A. Z. Direct estimation of polymer crystallinity with Raman spectroscopy using ratio of scattering cross-sections estimated from variable temperature measurements. *Spectrochim. Acta Part A Mol. Biomol. Spectrosc.* **224**, 117431 (2020).
49. Sundaram, R. S. *et al.* Electroluminescence in single layer MoS<sub>2</sub>. *Nano Lett.* **13**, 1416–1421 (2013).
50. Ghopry, S. A., Alamri, M. A., Goul, R., Sakidja, R. & Wu, J. Z. Extraordinary sensitivity of surface-enhanced Raman spectroscopy of molecules on MoS<sub>2</sub> (WS<sub>2</sub>) nanodomes/graphene van der Waals heterostructure substrates. *Adv. Opt. Mater.* **7**, 1801249 (2019).
51. Er, E. *et al.* High-yield preparation of exfoliated 1T-MoS<sub>2</sub> with SERS activity. *Chem. Mater.* **31**, 5725–5734 (2019).
52. Majee, B. P., Mishra, S., Pandey, R. K., Prakash, R. & Mishra, A. K. Multifunctional few-layer MoS<sub>2</sub> for photodetection and surface-enhanced raman spectroscopy application with ultrasensitive and repeatable detectability. *J. Phys. Chem. C* **123**, 18071–18078 (2019).
53. Jeong, H. Y. *et al.* Optical gain in MoS<sub>2</sub> via coupling with nanostructured substrate: Fabry-Perot interference and plasmonic excitation. *ACS Nano* **10**, 8192–8198 (2016).
54. Hu, J. Q., Shi, X. H., Wu, S. Q., Ho, K. M. & Zhu, Z. Z. Dependence of electronic and optical properties of MoS<sub>2</sub> multilayers on the interlayer coupling and Van Hove singularity. *Nanosc. Res. Lett.* **14**, 288 (2019).
55. Mouri, S., Miyauchi, Y. & Matsuda, K. Tunable photoluminescence of monolayer MoS<sub>2</sub> via chemical doping. *Nano Lett.* **13**, 5944–5948 (2013).
56. Plechinger, G. *et al.* Identification of excitons, trions and biexcitons in single-layer WS<sub>2</sub>. *Phys. Status Solidi Rapid Res. Lett.* **9**, 457–461 (2015).
57. Kwon, H. *et al.* Probing trions at chemically tailored trapping defects. *ACS Cent. Sci.* **5**, 1786–1794 (2019).
58. Zhu, Z. Y., Cheng, Y. C. & Schwingenschlögl, U. Giant spin-orbit-induced spin splitting in two-dimensional transition-metal dichalcogenide semiconductors. *Phys. Rev. B Condens. Matter Mater. Phys.* **84**, 153402 (2011).
59. Christopher, J. W., Goldberg, B. B. & Swan, A. K. Long tailed trions in monolayer MoS<sub>2</sub>: temperature dependent asymmetry and resulting red-shift of trion photoluminescence spectra. *Sci. Rep.* **7**, 1–8 (2017).
60. Lin, Z. *et al.* Controllable growth of large-size crystalline MoS<sub>2</sub> and resist-free transfer assisted with a Cu thin film. *Sci. Rep.* **5**, 1–10 (2015).
61. Liu, H. & Chi, D. Dispersive growth and laser-induced rippling of large-area singleglayer MoS<sub>2</sub> nanosheets by CVD on c-plane sapphire substrate. *Sci. Rep.* **5**, 1–8 (2015).
62. Splendiani, A. *et al.* Emerging photoluminescence in monolayer MoS<sub>2</sub>. *Nano Lett.* **10**(4), 1271–1275. <https://doi.org/10.1021/nl903868w> (2010).
63. Bano, A. & Gaur, N. K. Interfacial coupling effect on electron transport in MoS<sub>2</sub>/SrTiO<sub>3</sub> heterostructure: an ab-initio study. *Sci. Rep.* **8**, 1–8 (2018).
64. Zhang, J. *et al.* Observation of strong interlayer coupling in MoS<sub>2</sub>/WS<sub>2</sub> heterostructures. *Adv. Mater.* **28**, 1950–1956 (2016).
65. Tongay, S. *et al.* Thermally driven crossover from indirect toward direct bandgap in 2D semiconductors: MoSe<sub>2</sub> versus MoS<sub>2</sub>. *Nano Lett.* **12**, 5576–5580 (2012).
66. Mak, K. F. *et al.* Tightly bound trions in monolayer MoS<sub>2</sub>. *Nat. Mater.* **12**, 207–211 (2013).
67. Peimyoo, N. *et al.* Chemically driven tunable light emission of charged and neutral excitons in monolayer WS<sub>2</sub>. *ACS Nano* **8**, 11320–11329 (2014).
68. Choi, J., Zhang, H. & Choi, J. H. Modulating optoelectronic properties of two-dimensional transition metal dichalcogenide semiconductors by photoinduced charge transfer. *ACS Nano* **10**, 1671–1680 (2016).
69. Godefroo, S. *et al.* Classification and control of the origin of photoluminescence from Si nanocrystals. *Nat. Nanotechnol.* **3**, 174–178 (2008).
70. Hwang, J. D. *et al.* Suppressing the dark current of metal-semiconductor-metal SiGe/Si heterojunction photodetector by using asymmetric structure. *Thin Solid Films* **515**, 3837–3839 (2007).
71. Xu, H. Y. *et al.* Effects of annealing ambient on oxygen vacancies and phase transition temperature of VO<sub>2</sub> thin films. *RSC Adv.* **6**, 79383–79388 (2016).
72. Wang, L. *et al.* Oxygen vacancy induced room-temperature metal-insulator transition in nickelate films and its potential application in photovoltaics. *ACS Appl. Mater. Interfaces* **8**, 9769–9776 (2016).
73. Zaki, S. E. *et al.* Role of oxygen vacancies in vanadium oxide and oxygen functional groups in graphene oxide for room temperature CO<sub>2</sub> gas sensors. *Sensors Actuators A Phys.* **294**, 17–24 (2019).

74. Jain, S. K. *et al.* Effect of metal contacts on a GaN/Sapphire-based MSM ultraviolet photodetector. *J. Electron. Mater.* **47**, 6086–6090 (2018).
75. Casalino, M., Iodice, M., Sirleto, L., Rendina, I. & Coppola, G. Asymmetric MSM sub-bandgap all-silicon photodetector with low dark current. *Opt. Exp.* **21**, 28072 (2013).
76. Reddy, M. S. P., Kim, B.-J. & Jang, J.-S. Dual detection of ultraviolet and visible lights using a DNA-CTMA/GaN photodiode with electrically different polarity. *Opt. Exp.* **22**, 908 (2014).
77. Chao, C.-H., Weng, W.-J. & Wei, D.-H. Enhanced UV photodetector response and recovery times using a nonpolar ZnO sensing layer. *J. Vac. Sci. Technol. A Vac. Surf. Films* **34**, 02D106 (2016).
78. Ling, Z. P. *et al.* Large-scale two-dimensional MoS<sub>2</sub> photodetectors by magnetron sputtering. *Opt. Exp.* **23**, 13580 (2015).
79. Dhyani, V. & Das, S. High-speed scalable silicon-MoS<sub>2</sub> P-N heterojunction photodetectors. *Sci. Rep.* **7**, 44243 (2017).
80. Das, S., Chen, H. Y., Penumatcha, A. V. & Appenzeller, J. High performance multilayer MoS<sub>2</sub> transistors with scandium contacts. *Nano Lett.* **13**, 100–105 (2013).
81. Yang, Y., Huo, N. & Li, J. Sensitized monolayer MoS<sub>2</sub> phototransistors with ultrahigh responsivity. *J. Mater. Chem. C* **5**, 11614–11619 (2017).
82. Ko, P. J., Abderrahmane, A., Kim, N. H. & Sandhu, A. High-performance near-infrared photodetector based on nano-layered MoSe<sub>2</sub>. *Semicond. Sci. Technol.* **32**, 065015 (2017).
83. Zhuo, R. *et al.* High-performance self-powered deep ultraviolet photodetector based on MoS<sub>2</sub>/GaN p-n heterojunction. *J. Mater. Chem. C* **6**, 299–303 (2018).
84. Wu, J. M. & Chang, W. E. Ultrahigh responsivity and external quantum efficiency of an ultraviolet-light photodetector based on a single VO<sub>2</sub> microwire. *ACS Appl. Mater. Interfaces* **6**, 14286–14292 (2014).
85. Saenz, G. A., Karapetrov, G., Curtis, J. & Kaul, A. B. Ultra-high photoresponsivity in suspended metal-semiconductor-metal mesoscopic multilayer MoS<sub>2</sub> broadband detector from UV-to-IR with low Schottky barrier contacts. *Sci. Rep.* **8**, 1–11 (2018).
86. Liu, X. *et al.* All-printable band-edge modulated ZnO nanowire photodetectors with ultra-high detectivity. *Nat. Commun.* **5**, 1–9 (2014).
87. Choi, W. *et al.* High-detectivity multilayer MoS<sub>2</sub> phototransistors with spectral response from ultraviolet to infrared. *Adv. Mater.* **24**, 5832–5836 (2012).
88. Dhakal, K. P. *et al.* Confocal absorption spectral imaging of MoS<sub>2</sub>: optical transitions depending on the atomic thickness of intrinsic and chemically doped MoS<sub>2</sub>. *Nanoscale* **6**, 13028–13035 (2014).
89. Lopez-Sanchez, O. *et al.* Light generation and harvesting in a van der waals heterostructure. *ACS Nano* **8**, 3042–3048 (2014).

## Acknowledgements

The authors declare that they have received financial support from Scientific Research Projects Coordination (BAP)—Konya Necmettin Erbakan University (NEÜ), under Project Number: 191319007 that have appeared to influence the work reported in this paper. Moreover, the authors would like to thank the Science and Technology Research and Application Center (BITAM)—NEÜ for the continuous support through the characterizations section.

## Author contributions

M.A.B. suggested, designed and performed the whole experiments, characterizations, analysis, and writing the manuscript. S.E.Z. performed some experiments, characterization, and contributed for writing the manuscript. Y.R.E. and M.Y. contributed to writing, supervision, discussions and analysis of the data. M.S. characterized and analyzed the data, contributes to the plot of some figures, writing of the manuscript in addition to revision and editing.

## Competing interests

The authors declare no competing interests.

## Additional information

**Supplementary information** is available for this paper at <https://doi.org/10.1038/s41598-020-72990-9>.

**Correspondence** and requests for materials should be addressed to M.S.

**Reprints and permissions information** is available at [www.nature.com/reprints](http://www.nature.com/reprints).

**Publisher's note** Springer Nature remains neutral with regard to jurisdictional claims in published maps and institutional affiliations.



**Open Access** This article is licensed under a Creative Commons Attribution 4.0 International License, which permits use, sharing, adaptation, distribution and reproduction in any medium or format, as long as you give appropriate credit to the original author(s) and the source, provide a link to the Creative Commons licence, and indicate if changes were made. The images or other third party material in this article are included in the article's Creative Commons licence, unless indicated otherwise in a credit line to the material. If material is not included in the article's Creative Commons licence and your intended use is not permitted by statutory regulation or exceeds the permitted use, you will need to obtain permission directly from the copyright holder. To view a copy of this licence, visit <http://creativecommons.org/licenses/by/4.0/>.

© The Author(s) 2020